machines

MDPI

Article

Integrated Dynamic Modeling and Simulation of Wheeled Vehicle with Outer-Rotor In-Wheel Motors and Key Units

Xingyu Liu [1], Jixing Che [1], Jiulin Wu [1,2,*], Wei Jiang [1], Rui Liu [3] and Yihui Zhao [3]

[1] State Key Laboratory of Intelligent Manufacturing Equipment and Technology, Huazhong University of Science and Technology, Wuhan 430074, China; xyliu@hust.edu.cn (X.L.); chejx@hust.edu.cn (J.C.); jiangw@hust.edu.cn (W.J.)
[2] Guangdong Intelligent Robotics Institute, Guangzhou 510070, China
[3] Inner Mongolian First Machinery Group Co., Ltd., Baotou 014030, China; liurui617@sina.cn (R.L.); zihui182@163.com (Y.Z.)
* Correspondence: wujl@hust.edu.cn; Tel.: +86-18207178353

Abstract: The purpose of this paper is to accurately establish a model of a special vehicle driven by in-wheel motors (IWMs) and investigate its dynamic characteristics. This study proposes a novel integrated vehicle modeling strategy, focusing on the IWM and other key subsystems. Based on this strategy, the vehicle model is developed and simulated in ADAMS. The natural frequencies of the vehicle and transmission characteristics of key components are compared with MATLAB simulation results to validate the accuracy of the model. In the time-domain analysis, the vehicle system's time-domain characteristics are obtained by using random road spectra of different road grades as excitations. Our simulation results demonstrate that vibration input can be reduced by between 97% and 99% after multi-stage vibration reduction. This work will provide relevant parameters for the design of special vehicles driven by IWMs.

Keywords: in-wheel motor; dynamic model; mechanical system simulation; vibration isolation

check for updates

Citation: Liu, X.; Che, J.; Wu, J.; Jiang, W.; Liu, R.; Zhao, Y. Integrated Dynamic Modeling and Simulation of Wheeled Vehicle with Outer-Rotor In-Wheel Motors and Key Units. *Machines* **2024**, *12*, 624. https://doi.org/10.3390/machines12090624

Academic Editor: Dan Zhang

Received: 25 July 2024
Revised: 18 August 2024
Accepted: 3 September 2024
Published: 5 September 2024

Copyright: © 2024 by the authors. Licensee MDPI, Basel, Switzerland. This article is an open access article distributed under the terms and conditions of the Creative Commons Attribution (CC BY) license (https://creativecommons.org/licenses/by/4.0/).

1. Introduction

The development of internal combustion engines has a history of more than 100 years. Various vehicle types have been developed, including front-engine front-wheel drive, front-engine rear-wheel drive, mid-engine rear-wheel drive, and rear-engine rear-wheel drive [1]. The development of electric vehicles to replace traditional fuel vehicles has become an irreversible trend in the background of an energy crisis and environmental deterioration [2]. Electric vehicles can be a more promising alternative to the hitherto established combustion engine-propelled automobiles. Electric vehicles do not directly use any petroleum fuel, are quieter in operation, and require less maintenance and running costs [3].

In addition to the advantages mentioned above for electric vehicles, in-wheel motor (IWM)-drive vehicles possess superior dynamic performance, easy realization of active control, and a flexible vehicle body shape. Furthermore, vehicles driven by IWMs, which eliminate the mechanical transmission system and integrate fast and accurate multidimensional dynamic control, have brought significant attention in automotive industry [4–6].

The power unit is not only the power source of the vehicle but also the main vibration source in the vehicle [7]. The power source and vibration source of IWM vehicles are concentrated in the tires. The unique installation location and narrow installation space of IWMs make the working conditions harsh. To solve this problem, the advanced dynamic-damper mechanism [8–10] and active control methods [11–14], as well as design technology of the driving motor [15,16], were proposed.

There are many studies on the dynamics of IWMs and the vehicles driven by IWMs. In terms of IWM, IWM is known as the most ideal drive method for electric vehicles. The high-performance permanent magnet IWM is the power core of the electric drive system.

High corner power and mass torque density are key indicators to measure the performance of IWMs. In the field of civilian IWMs, Professor Hiroshi Shimizu of Keio University in Japan has produced various IWM-drive vehicles, such as IZA, ECO, KAZ, and Eliica (specific vehicle code) [17–19]. Lucid Air, introduced in 2022, has an electric motor that weighs only 31 kg, producing 500 kW. The complete drive unit comprises an electric motor, inverter, reduction gearset, and differential, collectively weighing 74 kg. In the field of military IWMs, the IWM products are mainly produced by German Magnet Motor (MM) and British QinetiQ and Magtech. They all use permanent magnet IWM transmission schemes. The IWM unit has superior power output abilities.

In terms of vehicle dynamics driven by IWMs, NVH (noise, vibration, and harshness) problems of the vehicle system are widely studied and continue to be of high interest and importance [20–23]. IWMs should satisfy the requirements for vibration mitigation and propulsion [24]. However, the use of IWMs causes the increased unspring mass load to increase suspension vibration [25]. Meanwhile, when any frequency of vibration is transferred to the human body, it is referred to as whole-body vibration (WBV) [26]. This vibration is known to cause physiological problems, including musculoskeletal, circulatory, and nervous issues; both acute and chronic injuries; and lower back pain [27]. Therefore, a great number of studies focused on vibration reduction of IWM suspension systems, reducing the unsprung mass of IWM-driven vehicles.

In Reference [28], the influence of vehicle speed on vertical vehicle vibration was studied [28]. After installing a bushing structure inside the IWM, Luo et al. established a quarter-vehicle vibration dynamics model to mitigate the increase in unsprung mass caused by motor magnetic gap (MMG) deformation [29]. Jin et al. developed an uncertain quarter-vehicle active suspension model with a dynamic damper IWM-drive system to improve the vibration performance and ride comfort of electric vehicles [30]. Nah et al. conducted a study on improving vehicle lateral stability and maneuverability by developing a vehicle stability controller through the establishment of an IWM vehicle model [31]. Drexler et al. established three types of whole-vehicle models. These models are based on a two-stage suspension structure, with electric motors used for tuning mass dampers and traditional hub motor designs [32]. The results indicate that the two-stage suspension increases body pitch and vertical acceleration under various driving conditions, while the acceleration of the motors and the lateral acceleration of the vehicle (especially during turning maneuvers) can be significantly reduced. There are many other studies on the dynamic modeling and analysis of IWM-driven vehicles [33–35]. These papers are based on the dynamics modeling and analysis of IWM-driven vehicles to optimize vehicle performance.

Lu et al. focused on a three-axis variable-structure DDUGV (Distributed-Drive Unmanned Ground Vehicle) and proposed a general dynamic modeling approach that considers terrain uncertainties and variable-structure parameters [36]. The dynamics research on multi-wheeled or unconventional DDUGVs primarily focuses on multi-wheel coordination control and steering analysis, while the analysis of their vertical dynamics is extremely limited [37–39]. There are many studies on the dynamics of IWMs and the vehicles driven by IWMs. There still appears to be some inadequacy in academic research regarding special vehicles driven by IWMs.

Special vehicles typically have a mass several times that of regular vehicles, leading to a higher unsprung mass for vehicles driven by IWMs. Additionally, special vehicles often operate on rough terrain, exacerbating the dynamic conditions of the entire vehicle (including the IWMs and other key subsystems). Addressing these challenges, a selection process for IWMs and the vehicles driven by them is discussed. Subsequently, an integrated modeling concept and strategy for the "environment–hub unit–suspension–vehicle body–vibration isolator–vibration-isolated body" system is proposed, and a dynamic model of the vehicle system is established in ADAMS (2018). The complete vehicle dynamics model is then validated using MATLAB (R2020b). Finally, the paper explores the dynamic characteristics of the vehicle.

2. In-Wheel Motor-Drive Vehicle System

2.1. Direct Drive In-Wheel Motors

In the IWM-drive vehicle system, the selection of the drive motor (IWM) is crucial. Vehicles, especially special vehicles, have stringent power requirements. The demand for power and performance of IWMs is increasing. The design requirements for IWMs mainly include the following aspects:

1. Power: The IWM should have higher power output to meet the demands of vehicle acceleration, climbing, and high-speed driving.
2. Efficiency: The motor design should be highly efficient, minimizing energy loss to maximize the vehicle's driving range.
3. Cooling: A well-designed and reliable cooling system is essential to prevent performance degradation or damage due to motor overheating.
4. Durability: The IWM should offer an extended motor life and reliable performance, with particular emphasis on the robustness of critical components, such as the bearing unit, which should be designed to minimize the risk of damage.

To meet the above design requirements, an IWM needs to be designed. The IWM is required to have a maximum torque of no less than 800 Nm. The design of the IWM is shown in Figure 1: One side of the stator is fixedly connected to the lower control arm of the suspension. The other side is connected to the outer ring of the hub bearing unit. The inner ring of the bearing is connected to the brake disc and the motor. The braking part is located on the stator structure to realize the braking effect by clamping the brake disc when necessary. The rim structure adopts a split scheme. One end of the rim is connected with the motor mover structure, and there is a vibration reduction structure between them. The tire is on the rim, and the support of the tire is realized through the action of the bracket.

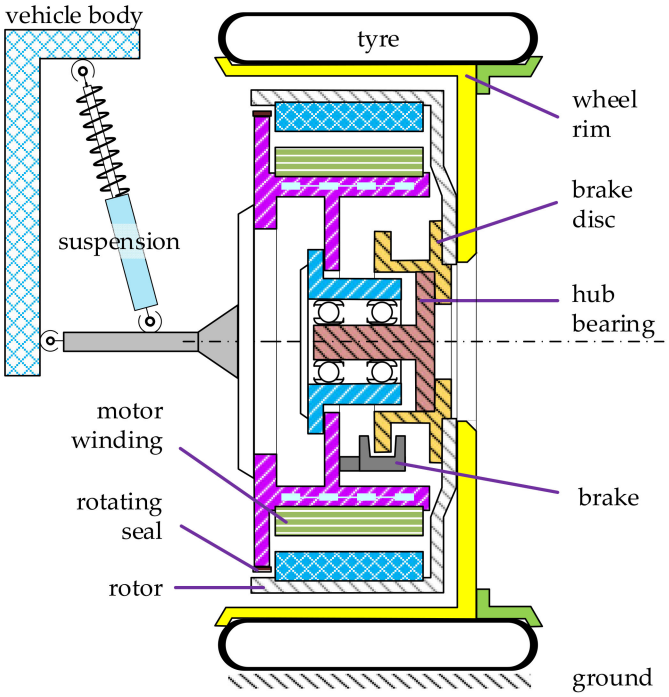


Figure 1. Design scheme of direct-drive in-wheel motor.

The IWM designed in this paper features an outer-rotor direct-drive configuration. The direct-drive outer-rotor IWM does not need a reduction device. The motor structure is simple, and the response speed is fast. The motor can stably output torque in a wide speed range. However, there are certain drawbacks to these types of IWMs, including average acceleration efficiency, high noise levels, and challenging working environments.

To address the above issues, the design of the stator slots employs a pear-shaped slot structure to increase slot area utilization. For the rotor magnetic circuit, a surface salient rotor structure is used, which has a lower manufacturing cost, simpler structure, and effectively reduces motor weight. Additionally, to optimize the sinusoidal waveform of the air-gap magnetic flux density of the permanent magnets, the maximum possible number of poles is selected, especially when the stator's inner diameter is constrained. Regarding motor efficiency, the motor can achieve over 96% efficiency at the rated operating point, and even at maximum torque, the efficiency remains above 92%, maintaining high efficiency across the entire operating range. For motor cooling, the most common water-cooling method is employed to control the temperature.

Table 1 provides the parameter specifications for the designed IWM. The prototype of the motor design has now been completed, and corresponding tests have been conducted. The experimental results indicate that the motor's performance meets the standards mentioned earlier and outlined in the tables.

Table 1. Design parameters of permanent-magnet synchronous IWM.

Structural Parameters	Values	Electrical Parameters	Values
Rotor outer diameter	384 mm	Rated current	57.7 A
Stator inner diameter	298 mm	Rated voltage	380 V
Number of slots	36	Rated torque	450 Nm
Number of poles	32	Rated speed	750 rpm
Air gap length	1 mm	Rated power	35.3 kW
Permanent magnet pole arc coefficient	0.86	Overload current	130 A
Winding turns	14	Overload torque	900 Nm
Lead wire diameter	0.88 mm × 13	Maximum efficiency	95.52%
Slot space-factor (pure copper)	0.68	Electric load	26.2 A/mm
Permanent magnet material	N40 EH	Current density	7.36 A/mm^2
Material of iron core	B35A250	D-Q inductance and resistance	0.970 mH/0.0646 Ω

2.2. Special-Wheeled Vehicle

In recent years, countries have been competing to develop special wheeled vehicles. Different from tracked vehicles, wheeled vehicles have the characteristics of speed and flexible responses. However, they have the disadvantage of a high failure rate when facing complex terrain. Wheeled armored vehicles generally use 6 × 6 or 8 × 8 drives.

As shown in Figure 2, the 6 × 6 wheeled vehicle model is designed and established in SolidWorks. The drive mode selects direct drive of each wheel. The suspension adopts three sets of MacPherson independent suspension systems. The 6 × 6 wheeled vehicle was chosen because it offers greater flexibility and more powerful output compared to a 4 × 4 wheeled vehicle. Additionally, it provides better reliability and easier coordination control compared to an 8 × 8 wheeled vehicle.

Here are the reasons for choosing the MacPherson independent suspension: simple structure, compact space utilization, cost-effectiveness, and durability. Despite the advantages of the MacPherson independent suspension, we must consider that its use in multi-axle military vehicles is relatively uncommon due to its potentially insufficient load capacity and durability for such applications. Additionally, under extreme and harsh road conditions, the performance of the MacPherson suspension may not match that of more complex suspension systems, such as hydraulic or air suspensions. Therefore, during the model construction, we performed a corresponding weight reduction on the car body to ensure its performance.

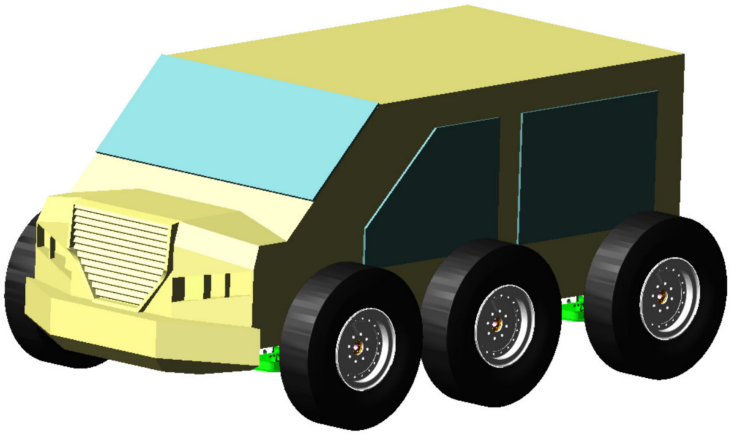


Figure 2. Special-wheeled vehicle model.

The quality of each component is shown in Table 2.

Table 2. Component quality parameter.

No.	Object		Value	Quantity	Unit
1	Motor system	Rotor	32.47	6	kg
2		Stator	46.63	6	kg
3	Gear trains	Gear trains	115.50	6	kg
4	Suspension system	Control arm	68.20	6	kg
5		Suspension	34.43	6	kg
6	Car body	Car body	3505.6	1	kg

3. Multi-Body Dynamics Modeling of Vehicle

In vehicle system dynamics, the objective is to improve both the dynamic performance and ride comfort through a vibration analysis and compensation [40]. To acquire the dynamic characteristic parameters of the vehicle driven by IWM, the initial step involves performing a vehicle dynamics modeling process within the ADAMS environment. The approach for vehicle dynamics modeling in ADAMS is to first propose a novel vehicle-integrated modeling strategy. Following this strategy, corresponding models for the IWM and other key subsystems are developed. Finally, spring–damper connections are established between the subsystems, completing the establishment of the final comprehensive vehicle dynamics model. MATLAB-based dynamic modeling is a relatively mature approach for vehicle dynamics modeling. MATLAB uses a straightforward and efficient equivalent method to establish the 1/n (where n refers to the number of vehicle tires) dynamic model of the vehicle.

3.1. Modeling of Vehicle in ADAMS

3.1.1. Vehicle-Integrated Modeling Strategy

Both the IWM and the occupants are facing complex working conditions and harsh environments. In order to establish a precise vehicle model driven by IWM in the modeling process, the analysis model should be constructed from a global perspective. In order to reflect the influence of different system characteristics on the drive characteristics of the IWM, a new comprehensive strategy for global system modeling "road environment–hub unit–suspension–vehicle body–vibration isolator–vibration-isolated body" is proposed in Figure 3.

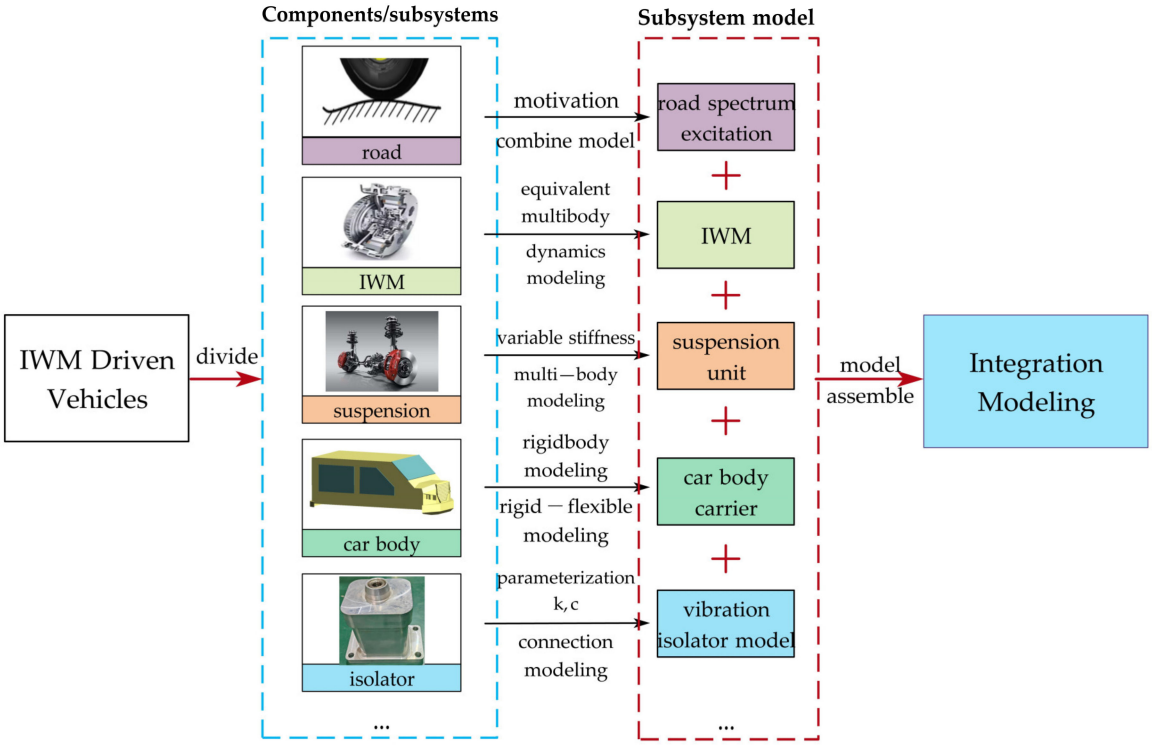


Figure 3. Schematic diagram of system-integrated modeling strategy for special vehicles.

The integrated modeling strategy for system comprehensive performance can be divided into two main parts: subsystem equivalence modeling and subsystem model assembly.

Subsystem equivalence modeling equates the vehicle to a spring–damping model based on information such as road conditions and vehicle speed. The excitation of the vehicle on the road surface is equivalent to the road spectrum excitation. For other structures or subsystems in the vehicle system, they are equated to structural sub-models based on their respective mechanical properties and topological relationships.

The main task of the sub-model stage is to form the final system dynamics model after organic assembly according to the constructed subsystem models. On the basis of the model of each component/subsystem, it can be reorganized according to its topological relationship and connection characteristics in the original system. Then, its system-integrated model can be constructed. In the process of sub-model assembly, it is necessary to consider the topological connection relationship that is cut off when the subsystem is divided. And it is equivalent to a connection model to connect the two subsystem models to which the original connection structure belongs.

In the system dynamics model constructed by the system-integrated modeling strategy, the characteristics of each key component/subsystem are expressed consistently and organically in the model.

It is worth noting that, although this novel vehicle-integrated modeling strategy is developed based on the dynamic modeling of a specific type of special vehicle, it can be adapted for the dynamic modeling of various types of IWM-driven special-wheeled vehicles.

3.1.2. Modeling of In-Wheel Motor

In traditional fuel-driven vehicles, the engine serves not only as the power source but also as the primary vibration source. In contrast, the electric motor in electric vehicles merely serves as a power source, with its impact on external vibration output considered negligible. However, for vehicles driven by IWMs, the increased unsprung mass and exposure to road-surface vibrations deteriorate the internal dynamic environment of the IWMs. Therefore, dynamic modeling of IWMs holds significant importance.

In order to construct an accurate dynamic model of an IWM-driven vehicle, this section builds an IWM dynamic model around the IWM bearing unit and conducts a simulation analysis in Section 4.1.

In terms of structural dynamic characteristics, the modal properties of key structural elements are crucial due to their natural vibration characteristics. These modal properties play a significant role in the overall vibration transmission and the time–frequency-domain vibration response of the system. For research purposes, the bearing unit is simplified as a rigid element connecting the stator and rotor. This section primarily focuses on the modal characteristics of stator and rotor.

The hub bearing unit is equivalent to a mass-spring–damping system, as shown in Figure 4. The inner ring and the outer ring of the bearing are constructed as rigid parts. The radial support stiffness and damping effect of the bearing are mainly considered between the inner ring and the outer ring (spring–damper).

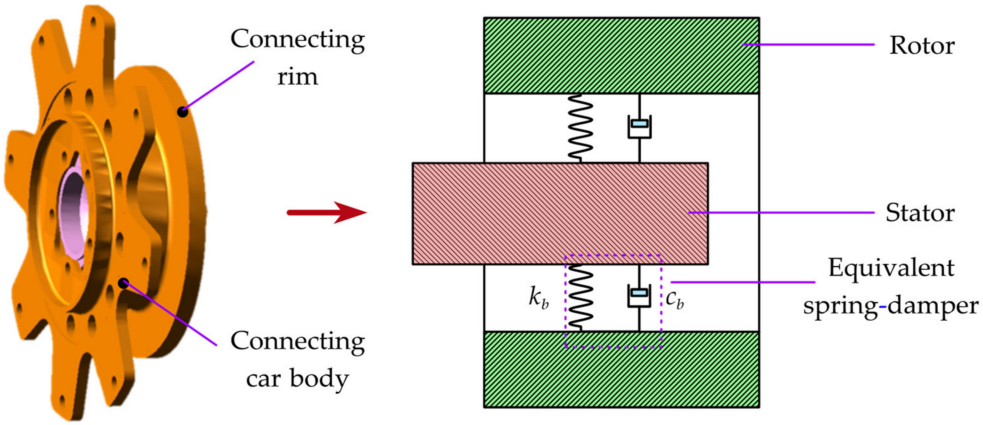


Figure 4. Dynamic modeling of hub bearing units.

The rotor consists of a frame, surface-mounted magnets, a brake disk, and corresponding fixed components. The surface-mounted magnets are solidly connected to the rotor frame by welding adhesive, and the arrangement is in the form of N-S staggered arrays. The stator is an integral structure, primarily composed of a frame, a bracket, and a limiting ring. The rotor and stator are imported into the finite element analysis (FEA) software for intrinsic characterization. The rotor-frame material is structural steel, the magnet material is rubidium iron boron, the stator-frame material is also structural steel, and the material property in Table 3.

Table 3. Material properties.

Material	Poisson's Ratio	Density (g/cm^3)	Modulus of Elasticity (GPa)
RbFeB	0.25	7.5	160
Stainless steels	0.28	7.85	210

It is worth noting that the dynamic model established in this study is based on this particular IWM. However, this approach can be extended to other direct-drive outer-rotor IWMs. Although this may result in slight deviations in model accuracy, the simplification methods and related principles for the motor can still be applied.

3.1.3. Modeling of Key Subsystems

According to the vehicle-integrated dynamics modeling strategy, the dynamics modeling work, including IWM bearing units, is carried out.

The modeling of the hub bearing unit is completed in Section 3.1.2.

The tire system is dynamically modeled in the same way. It is equivalent to a mass-spring–damper system. The results are shown in Figure 5. The rim and tire are constructed as rigid components. Their interactions with the ground are constructed as an equivalent 3-DOF (degree of freedom) spring–damper in order to characterize the elastic action of the tire in different directions.

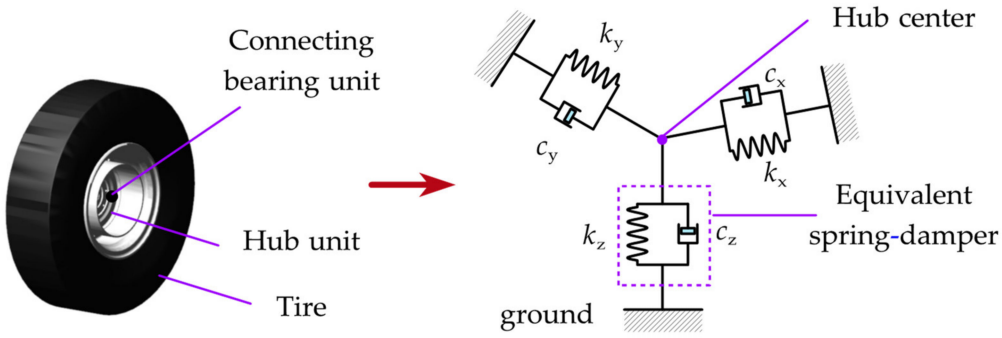


Figure 5. Dynamic modeling of tire subsystems.

The schematic diagram of the structure modeling of the suspension part is shown in Figure 6 for during the modeling process. In this part, the vibration damping performance of the suspension is mainly considered. The steering part is ignored.

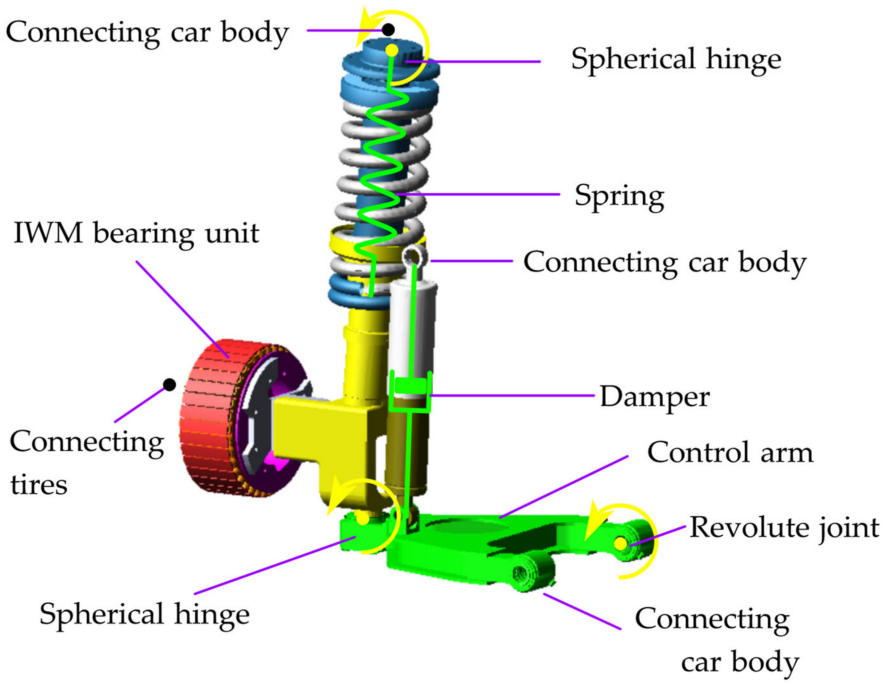


Figure 6. Dynamic modeling of suspension subsystems.

Before establishing the suspension system in ADAMS, it is necessary to appropriately simplify the 3D model by separating the suspension spring and damper. The damper is divided into two parts: the upper damper and the lower damper, with a translational joint applied between them to ensure vertical movement. Similarly, the suspension spring is divided into the spring and the sliding column (kingpin).

The upper end of the suspension spring is connected to the vehicle body with a spherical joint, while the lower end of the strut is also connected to the control arm with a spherical joint. The upper damper is connected to the vehicle body via a revolute joint, and the lower damper is connected to the control arm with another revolute joint. The lower end of the strut is fixedly connected to the IWM.

3.1.4. Comprehensive Vehicle Dynamics Modeling

Then, on the basis of the key units dynamic modeling, the models are assembled according to the topological relationship to build a vehicle-integrated dynamics model. To ensure the accuracy of the vehicle model in ADAMS, it is crucial to perform reasonable equivalence. In this section, a 1/6 ADAMS dynamic model of the vehicle is first established, with the specific equivalent model shown in Figure 7.

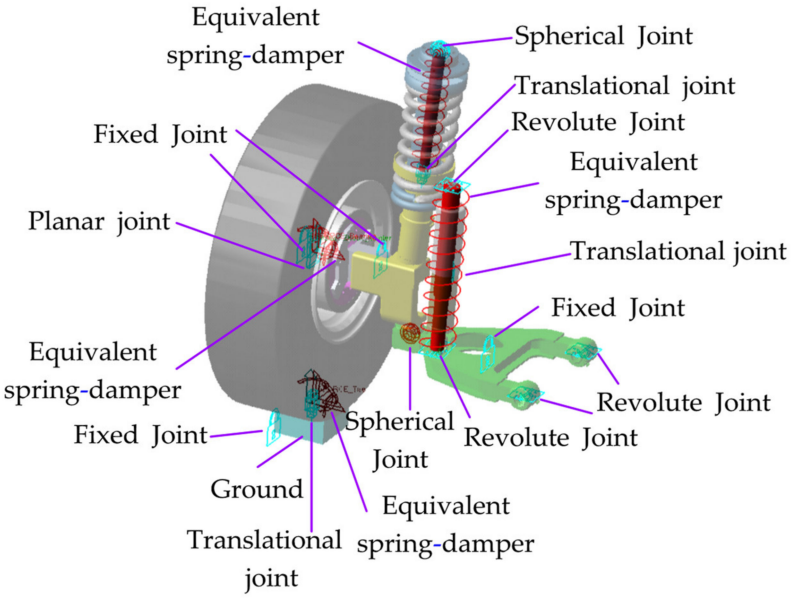


Figure 7. The 1/6 vehicle dynamics modeling in ADAMS.

Figure 8 shows a diagram of the vehicle dynamics model. In the process of equivalent modeling, the vehicle body, stator unit, motor unit, and rim structure are all equivalent to rigid units. The suspension system, bearing support, damping structure, and gear train are equivalent to elastic units with stiffness and damping characteristics. For stiffness equivalence, the design of a vehicle's suspension and tires is not as simple as making them perpendicular to the ground. During the design process, parameters such as the camber angle, caster angle, and kingpin inclination must also be considered. In this model, the camber angle is set at 5°, the caster angle at 3°, and the kingpin inclination at 7°. Setting the camber angle improves the vehicle's steering performance and reduces tire wear. The caster angle enhances straight-line stability, which is particularly important during high-speed driving. The kingpin inclination helps reduce steering effort and improves the self-centering characteristics of the steering system. Although this paper does not focus on the vehicle's steering, the angles of the wheels and suspension affect their stiffness, which must be considered when establishing the vehicle dynamics model.

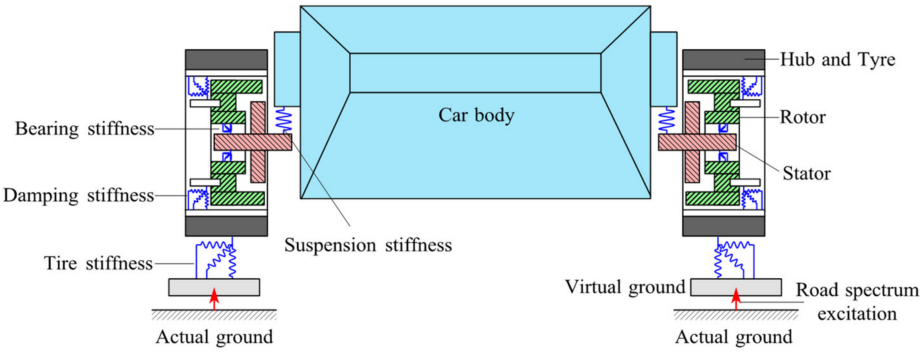


Figure 8. Equivalent multi-body modeling considering the entire vehicle.

Based on the vehicle modeling strategy and modeling scheme, the subsystems are connected into the whole system by different connecting units with the help of dynamic simulation software ADAMS. The mass properties of each component are obtained by CAE (Computer-Aided Engineering) software based on the 3D model. In addition, in order to facilitate the analysis of the specific parameters on the dynamic characteristics and the optimization of key parameters, design variables are used for key parameters, such as suspension springs, bearing equivalent stiffness, damping structure stiffness, and tire stiffness. Then, the analysis and optimization methods are carried out. The values of the parameters in the model can be modified by the values of the design variables. Finally, under the MSC ADAMS, a multi-body dynamics vehicle model is constructed, as shown in Figure 9. The equivalent multibody dynamic model contains a total of 49 rigid-body components and 60 connection and constraint pairs, with a total of 36 degrees of freedom.

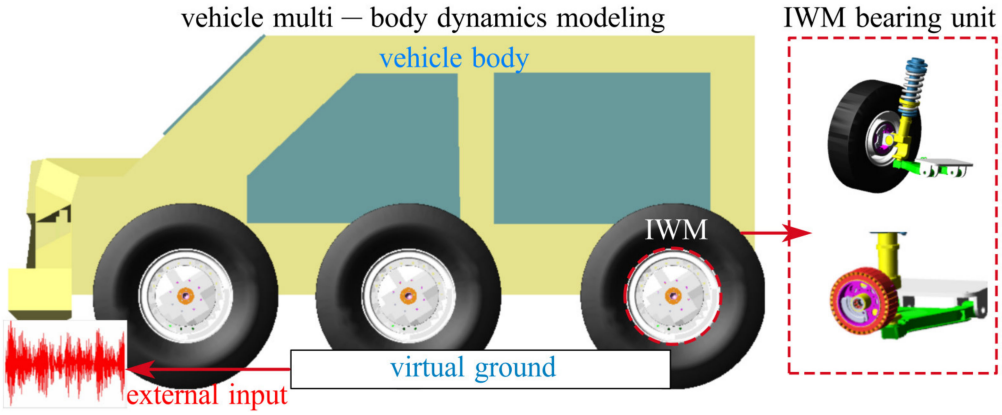


Figure 9. Vehicle system dynamics model in ADAMS environment.

It is worth noting that the dynamic model established in this paper is based on the MacPherson independent suspension. However, this approach can be extended to other 6×6 IWM direct-drive wheeled vehicles. Although this method might lead to some minor deviations in model accuracy, the simplification techniques and related principles for key vehicle components remain applicable. For dynamic modeling of 4×4 or 8×8 IWM direct-drive wheeled vehicles, it will be necessary to adjust the number of drive wheels accordingly. If a different suspension type (such as double wishbone or air suspension) is used, a separate dynamic model for the new suspension system will need to be developed to replace the existing suspension model.

3.2. Modeling of Vehicle in MATLAB

In order to model vehicle dynamics in MATLAB, Figure 10a shows a schematic diagram of multi-body modeling of a 1/6 vehicle model. In Figure 10, m_c is the sprung mass, (body mass); k_c and c_c are the stiffness and damping of the vehicle suspension; m_w is the mass of the tire subsystem; m_{ms} is the mass of the IWM stator; m_{mr1} and m_{mr2} are the masses of the IWM rotor; k_w and c_w are the stiffness and damping of the tire; k_{mr1}, k_{mr2}, c_{mr1}, and c_{mr2} are the stiffness and damping of the bushings between the rotor and the tire; k_m is the stiffness of the hub bearing unit; F is the interaction force of the motor; x_r is the excitation displacement of the ground; x_w is the wheel displacement; x_s is the vehicle body displacement; x_{mr1} and x_{mr2} are the displacements of the motor; and x_{ms} is the displacement of the stator.

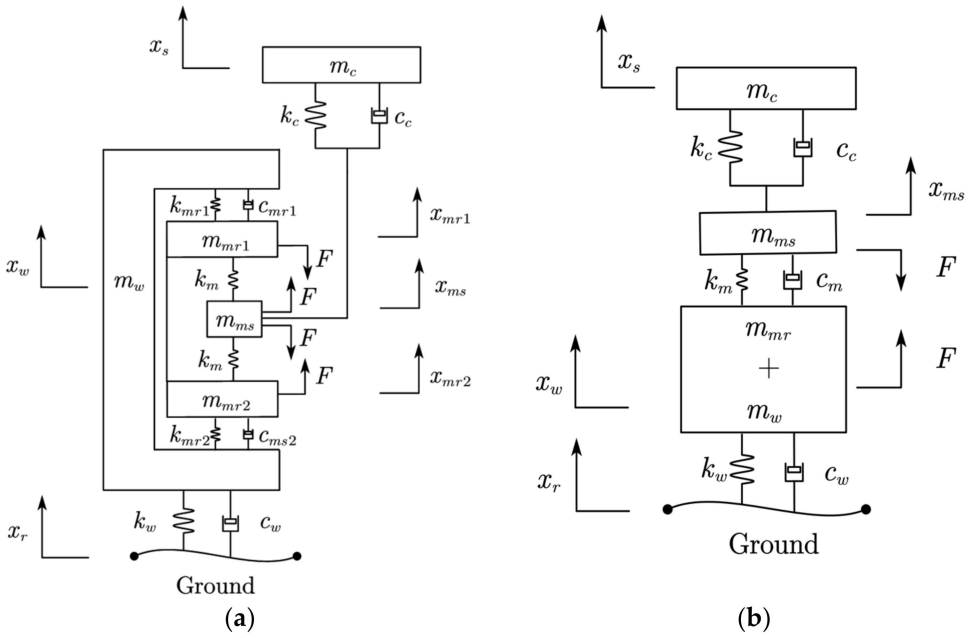


Figure 10. (**a**) The 1/6 vehicle model multi-body modeling. (**b**) The simplified 1/6 vehicle model multibody modeling.

Figure 10a is simplified to Figure 10b. The vehicle dynamics system described above can be viewed as a linear system. The description of a linear system can be represented using differential equations, transfer functions, and state-space representation. Among these, differential equations and transfer functions cannot fully reveal the complete dynamic behavior of the system. In this paper, the state-space representation method is chosen. This approach can reflect changes in all independent variables of the system and determine the internal dynamic states of the system.

The equation of motion in Figure 10b can be derived as follows [41]:

$$c_w\left(\dot{x_r} - \dot{x_w}\right) + k_w(x_r - x_w) + c_m\left(\dot{x_{ms}} - \dot{x_w}\right) + k_m(x_{ms} - x_w) + F = (m_w + m_{mr})\ddot{x_w} \quad (1)$$

$$c_m\left(\dot{x_w} - \dot{x_{ms}}\right) + k_m(x_w - x_{ms}) + c_c\left(\dot{x_s} - \dot{x_{ms}}\right) + k_c(x_s - x_{ms}) - F = m_{ms}\ddot{x_{ms}} \quad (2)$$

$$m_c\ddot{x_s} + c_c\left(\dot{x_s} - \dot{x_{ms}}\right) + k_c(x_s - x_{ms}) = 0 \quad (3)$$

Perform the Fourier transform on the equation above:

$$x_w\left[-\omega^2(m_w + m_{mr}) + j\omega(c_w + c_m) + k_w + k_m\right] = x_{ms}(j\omega c_m + k_m) + x_r(j\omega c_w + k_w) \quad (4)$$

$$x_{ms}\left[-\omega^2 m_{ms} + j\omega(c_m + c_c) + k_m + k_c\right] = x_w(j\omega c_m + k_m) + x_s(j\omega c_c + k_c) \quad (5)$$

$$x_s\left(-\omega^2 m_c + j\omega c_c + k_c\right) = x_{ms}(j\omega c_c + k_c) \quad (6)$$

Then, list the vehicle simplified model from bottom to top, including the mass, stiffness, and damping matrices:

$$[m] = \begin{bmatrix} m_w + m_{mr} & 0 & 0 \\ 0 & m_{ms} & 0 \\ 0 & 0 & m_c \end{bmatrix} \quad (7)$$

$$[k] = \begin{bmatrix} k_w + k_m & -k_m & 0 \\ -k_m & k_m + k_c & -k_c \\ 0 & -k_c & k_c \end{bmatrix} \quad (8)$$

$$[c] = \begin{bmatrix} c_w + c_m & -c_m & 0 \\ -c_m & c_m + c_c & -c_c \\ 0 & -c_c & c_c \end{bmatrix} \tag{9}$$

The natural frequency of the vehicle system is a physical characteristic determined by factors such as its structure, size, and shape. This physical characteristic does not change whether the object is in a state of vibration or not. The natural frequency can be expressed as follows:

$$\left([k] - \omega^2[m]\right)\{u\} = \{0\} \tag{10}$$

This is a system of multivariable linear homogeneous algebraic equations concerning $\{u\}$.

$$\Delta\left(\omega^2\right) = \begin{bmatrix} k_w + k_m - \omega^2(m_w + m_{mr}) & -k_m & 0 \\ -k_m & k_m + k_c - \omega^2 m_{ms} & -k_c \\ 0 & -k_c & k_c - \omega^2 m_c \end{bmatrix} = 0 \tag{11}$$

It is worth noting that there are inaccuracies in the dynamic equivalent representation, as shown in Figure 10b. As depicted in Figure 11, the actual location of the equivalent spring model should be between the vehicle body and the IWM bearing unit, rather than directly above the IWM bearing unit.

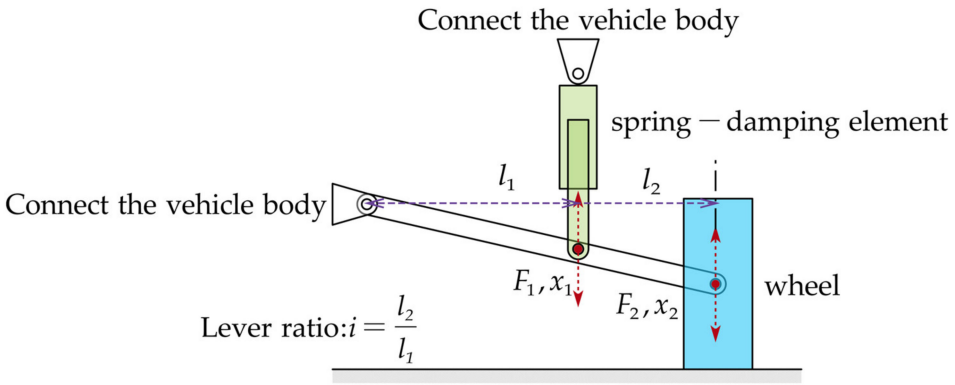


Figure 11. Wheel–suspension relationship for special vehicle with IWM.

Due to the presence of a leverage ratio in the suspension, there exists a conversion relationship between wheel loads and suspension loads, as well as between wheel displacement and suspension displacement. Figure 11 illustrates the wheel–suspension relationship diagram for a special vehicle with IWM.

The leverage ratio is i. It can be seen that when the leverage ratio, i, is less than 1, the wheel displacement surpasses the suspension displacement, and the suspension load surpasses the wheel load. Furthermore, from the stiffness definition, it can be obtained:

$$k_1 = -\frac{\Delta F_1}{\Delta x_1} = -i^2 \frac{\Delta F_2}{\Delta x_2} = i^2 k_2 \tag{12}$$

where l_1, k_1, and F_1 represent, respectively, the distance from the vehicle's suspension to the vehicle body, the stiffness of the vehicle's suspension, and the force at the vehicle's suspension; and l_2, k_2, and F_2 represent, respectively, the distance from the vehicle's suspension to the tire, the overall stiffness, and the equivalent force of the suspension.

From Equation (12), it can be observed that the suspension stiffness is i^2 times the converted overall stiffness of the wheel. When the leverage ratio, i, is less than 1, the converted overall stiffness is less than the suspension stiffness.

4. Analysis of Vehicle Dynamics

The dynamic analysis of the vehicle system includes the natural characteristics of the system, the vibration of key parts of the vehicle, the transmission characteristics of the ground vibration, and the time-domain characteristics of the vehicle.

This section employs frequency-domain vibration analysis to obtain the vibration mode of important orders of the whole vehicle and the vibration transmission characteristics among key parts. To validate the accuracy of the theoretical model, the vibration modes obtained from solving the vehicle's ADAMS model and the transmission characteristics of ground vibration are compared with the solutions from the MATLAB model. Additionally, the impact of subsystem units, such as the hub unit and suspension unit, on the overall vehicle vibration is analyzed under different isolation parameter configurations. Furthermore, optimization targets that can enhance the isolation performance of the IWM system and the overall vehicle damping system are extracted. The parameters of the important components of the special vehicle model are shown in Table 4.

Table 4. Main parameters of the vehicle integrated model.

No.	Parameter Category	Object	Parameter Name	Numerical	Units
1	Quality parameter	Motor system	Motor system quality	Table 1 Component quality parameter	kg
2		Gear train	Gear train quality		kg
3		Suspension system	Suspension system quality		kg
4		Vehicle body	Vehicle body quality		kg
5	Kinetic parameter	Suspension	Suspension spring	85	N/mm
6			Suspension damping	1	N.S/mm
7		Gear train	Tire radial stiffness	1000	N/mm
8			Tire radial damping	0.2	N.S/mm
9			Tire side stiffness	250	N/mm
10			Tire side damping	0.2	N.S/mm
11			Tire circumferential stiffness	1000	N/mm
12			Tire circumferential damping	0.2	N.S/mm

4.1. Frequency-Domain Characteristic Analysis

4.1.1. Natural Frequency

- Vehicle

The natural frequency of the whole vehicle is analyzed in ADAMS/View. The modal results of the whole vehicle are shown in Table 5. On the basis of the existing vehicle vibration model, the corresponding modal analysis of the vehicle is carried out, and a total of 36 modes are obtained, of which there are six modes related to the vehicle body. It can be seen from the table that the translational and rotational modes of the body are the first three modes. The rotational modes of the vehicle are from the 4th mode to the 6th mode, and the first six modal frequencies are roughly distributed between 1 and 4 Hz. In step mode 3, the frequency of the car body translation around the Y axis is 1.47 Hz.

$$f = \frac{\sqrt{\omega^2}}{2\pi} \tag{13}$$

From Equations (10)–(13), the results of the natural frequencies, f, are as follows: $f_1 = 1.4725$ Hz, $f_2 = 5.9839$ Hz, and $f_3 = 267.4109$ Hz.

f_1 is 1.4725 Hz, which means that the frequency of the car body translation around the Y axis is primarily influenced by the vehicle suspension, and the modeling in ADAMS and MATLAB is consistent.

Table 5. Vehicle modal analysis.

Step Mode	Vibration Mode Description	Damp Ratio	Frequency (Hz)
1	The car body rotates around the Z axis	0.025	0.94
2	The car body rotates around the X axis	0.027	1.14
3	The car body translation around the Y axis	0.038	1.47
4	The whole vehicle rotates around the Y axis	0.004	2.26
5	The whole vehicle rotates around the Z axis	0.002	2.58
6	The whole vehicle rotates around the X axis	0.016	4.30

- Rotor and Stator

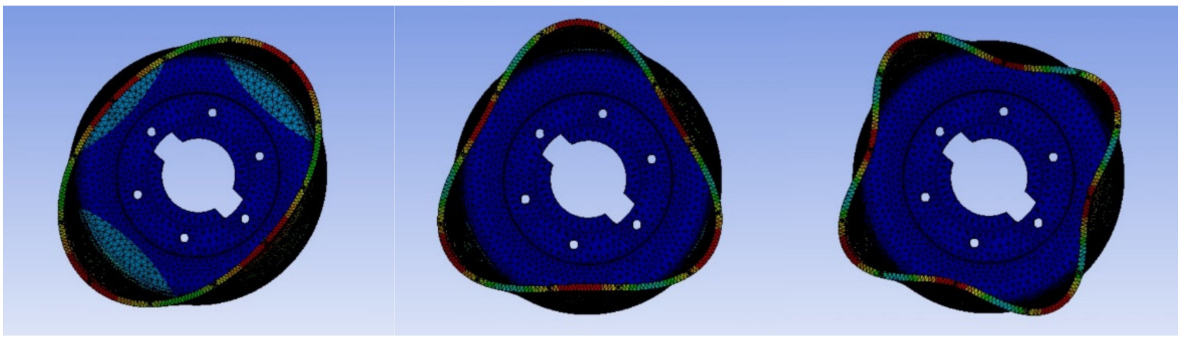
The dynamic environment inside IWM is quite harsh. During vehicle dynamics analysis, the modes of the stator and rotor should be avoided from coinciding with the vehicle modes to reduce the impact of resonance on the IWM and the vehicle.

Since the rotor of the IWM is a rotating body part, its end face is prone to bending under external impacts. In the modal analysis, the focus is on the free modes of the rotor end face. The free boundary is used in the rotor modal simulation analysis, and the calculation order is set to 20 orders. This contains rigid body modes of six orders and fixed-end face modes of at least three orders, and after excluding these modes, the third-order modes of the motor rotor end face are extracted as shown in Table 6.

Table 6. Rotor modal frequency simulation table.

Order	Simulation Frequency (Hz)	Vibration Pattern
1	263.24	Ellipses
2	612.72	Hexagon
3	1045.30	Octagon

The third-order frequency of the modal frequency of the rotor end face part is not zero, which is statistically shown in Table 6. The simulation frequency of the first order is 263.24 Hz, and the vibration pattern is elliptical (Figure 12a); the simulation frequency of the second order is 612.72 Hz, and the vibration pattern is hexagonal (Figure 12b); and the simulation frequency of the third order is 1045.30 Hz, and the vibration pattern is octagonal (Figure 12c).



(**a**) (**b**) (**c**)

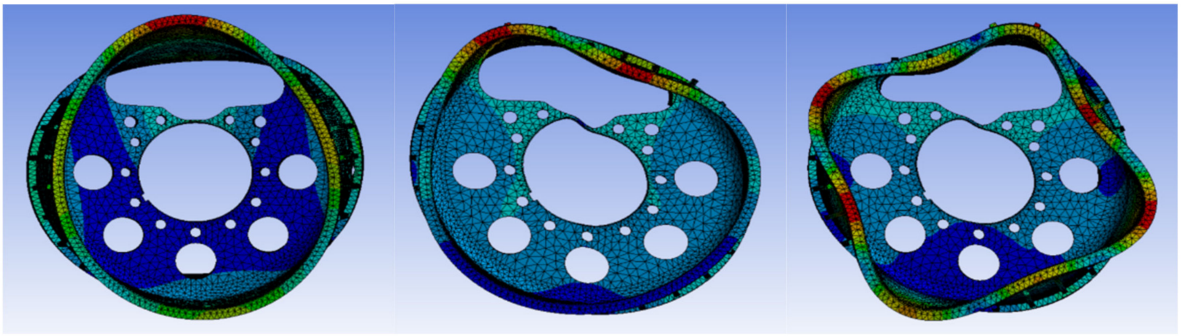
Figure 12. (**a**) First-order vibration pattern of rotor. (**b**) Second-order vibration pattern of rotor. (**c**) Third-order vibration pattern of rotor. Blue indicates minimal deformation, while red indicates maximum deformation.

The free boundary is used in the stator modal simulation analysis, and the calculation order is set to 20 orders. This contains rigid-body modes of six orders and fixed end-face modes of at least three orders; after excluding these modes, the third-order modes of the extracted motor stator are shown in Table 7.

Table 7. Stator modal frequency simulation table.

Order	Simulation Frequency (Hz)	Vibration Pattern
1	821.94	Ellipses
2	1403.00	Quadrilateral
3	2365.20	Octagon

The simulation frequency of the first order is 821.94 Hz, and the vibration pattern is elliptical (Figure 13a); the simulation frequency of the second order is 1403.00 Hz, and the vibration pattern is quadrilateral (Figure 13b); and the simulation frequency of the third order is 2365.20 Hz, and the vibration pattern is octagonal (Figure 13c).



(**a**) (**b**) (**c**)

Figure 13. (**a**) Stator first-order vibration patterns. (**b**) Stator second-order vibration patterns. (**c**) Stator third-order vibration patterns. Blue indicates minimal deformation, while red indicates maximum deformation.

In ADAMS/View, the vehicle's vibrations around the bearing unit are concentrated in the range from the 31st to 36th orders. Among them, the highest frequency is at the 36th order, with a frequency of 239.989 Hz. If this frequency is close to the first-order frequency of the rotor, it may lead to resonance. However, the actual experimental result is at 282.50 Hz. Based on this analysis, the strength of the motor can be verified. This test also contributes to the modeling of dynamic units and the dynamic research of IWMs and special vehicles.

4.1.2. Vibration Transmissibility

This section primarily focuses on the transfer relationships between the vehicle body and the ground, as well as between the vehicle's bearing unit and the ground. The computation of magnitude–frequency characteristics under various typical damping ratios were performed using MATLAB for analysis.

From Equations (4)–(6), we can derive the following:

$$\left|\frac{x_s}{x_r}\right| = \gamma\left[\frac{1+4\xi^2\lambda^2}{\Delta}\right]^{\frac{1}{2}} \tag{14}$$

$$\Delta = \left\{\left[1-(\omega/\omega_0)^2\right]\left[1+\gamma-\frac{1}{\mu}(\omega/\omega_0)^2\right]-1\right\}^2 + 4\xi^2(\omega/\omega_0)^2\left[\gamma-(\frac{1}{\mu}+1)(\omega/\omega_0)^2\right]^2 \tag{15}$$

where γ represents the stiffness ratio, μ represents the mass ratio, ξ represents the damping ratio, and λ represents the frequency ratio.

The MATLAB analysis results are shown in Figures 14 and 15.

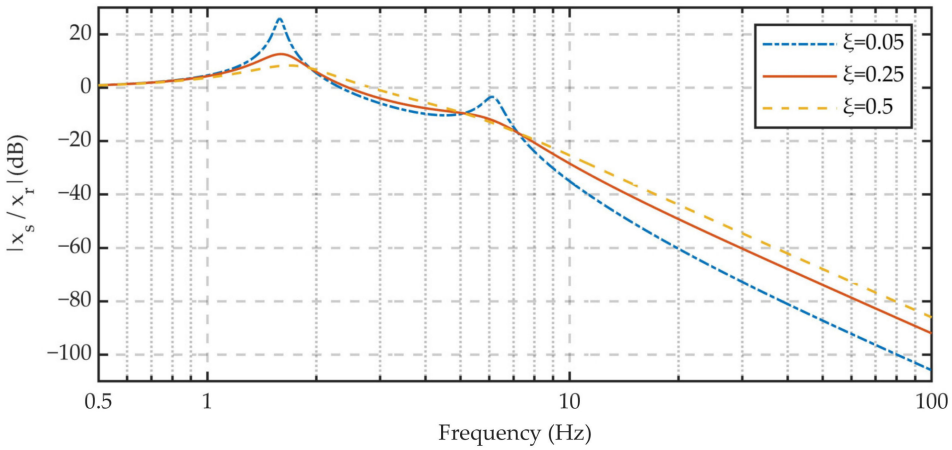


Figure 14. Suspension–road relationship for special vehicle with IWM.

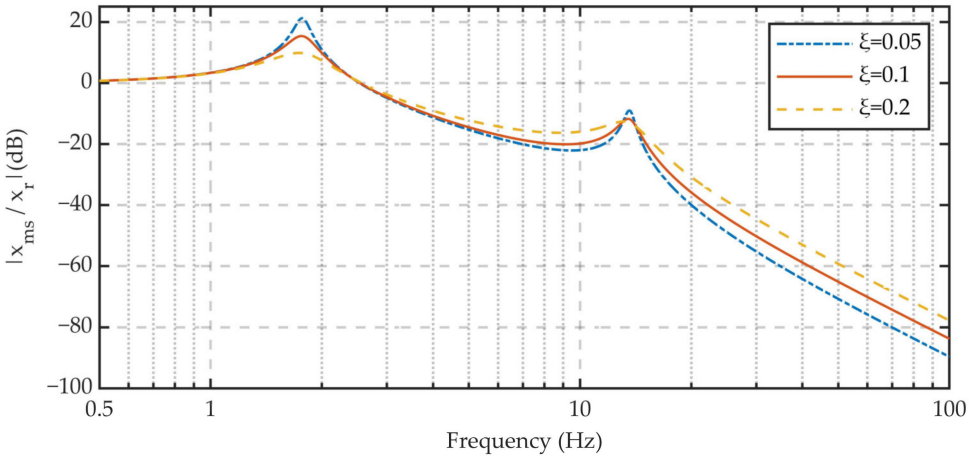


Figure 15. Bearing unit–road relationship for special vehicle with IWM.

In ADAMS/View, the main indicator analyzed in this work is the vertical vibration transmissibility of the critical transmission path. The transmissibility is the acceleration ratio.

Regarding the analysis of the vibration transfer characteristics of the whole vehicle, the excitation equipment is the vehicle power equipment (IWM unit). The excitation points are selected as a total of six excitation points at the centroid position of each rotor. The right three groups are selected, each named as input right front wheel, input right middle wheel and input right rear wheel. When different excitations are input, fix the corresponding tire to the ground. The response points are selected as shown in Table 8.

Table 8. Response measurement point location description.

Measurement Reference Point	Position
Output—right rear	Farthest rear right point of the vehicle
Output—right front	Farthest front right point of the vehicle
Output—left rear	Farthest rear left point of the vehicle
Output—left front	Farthest front left point of the vehicle
Output—centroid	Center of mass of the vehicle

Set the amplitude of the centroid of the motor rotor to 1 g and test the vibration frequency domain from 0.1 Hz to 100 Hz. The vertical acceleration is measured at five different points on the vehicle body to obtain the transfer characteristics under different parameter groups. The vertical vibration transmissibility of each measurement point is shown in Figures 16–18.

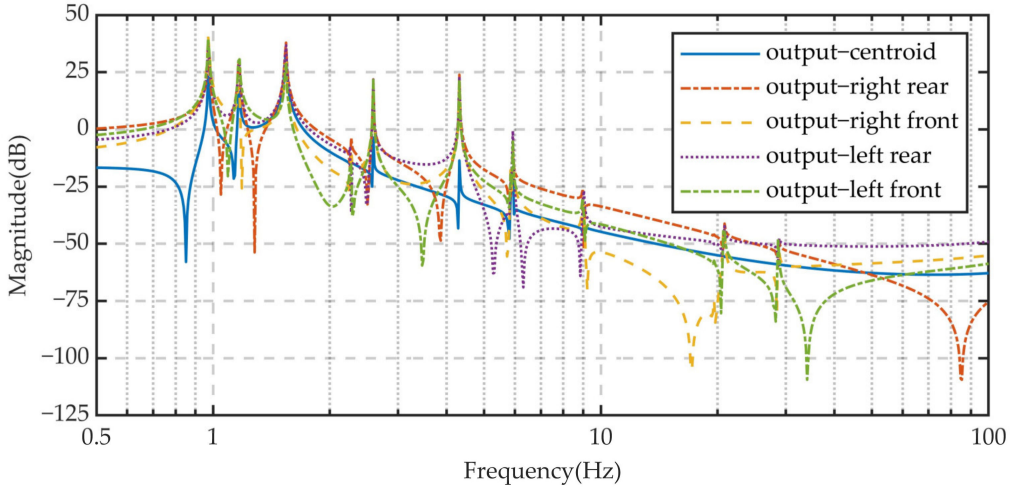


Figure 16. Input vibration transmission of right rear wheel.

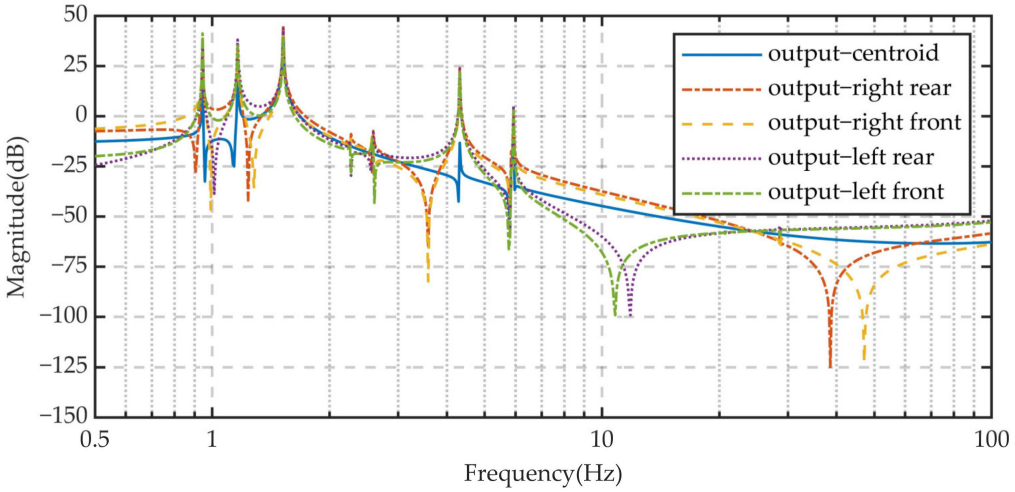


Figure 17. Input vibration transmission of right middle wheel.

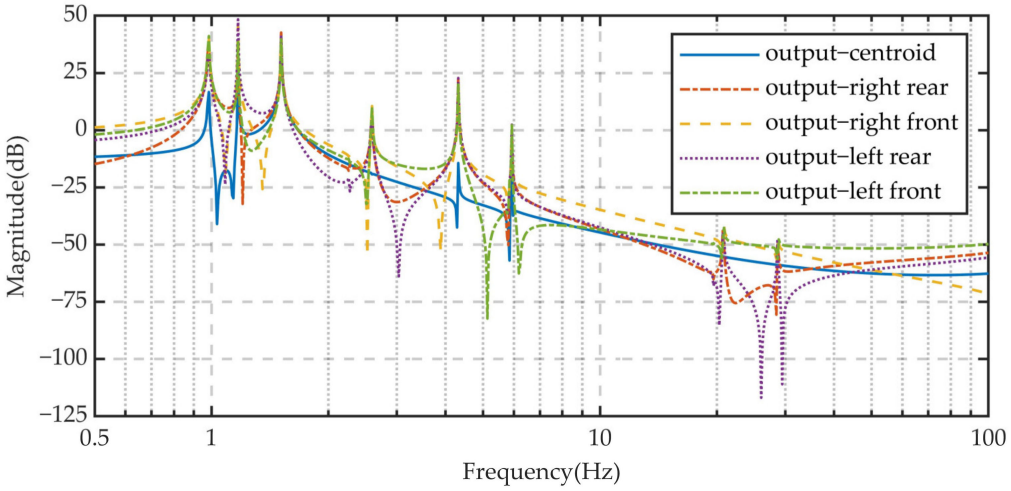


Figure 18. Input vibration transmission of right front wheel.

From Figure 16, we can see that the vibration transfer of the vertical acceleration from the wheel motor to the vehicle body mass center (mass center) is low within 1 Hz. At 0.1 Hz, the maximum difference between the response of other excitation points and the response of the mass center excitation point is 15 dB. Additionally, the maximum difference between the response of other excitation points and the response of the mass center excitation point is up to 60 dB.

Different from the traditional engine drive, this model is driven by each wheel motor. From the analysis results in Figure 16, it can be obtained that the vibration transmission of the vehicle body center of mass under low-frequency conditions is significantly lower than the other vibration transmission paths. When the single-wheel excitation is input, the position of the center of mass of the vehicle body is more stable. On the contrary, the response points, such as the right front and left front of the vehicle body, show a relatively high vibration transmission rate, and the stability of this part is insufficient.

From the analysis results, it can also be observed that the vertical acceleration vibration transmissibility curves from the engine to each part of the vehicle body have significant fluctuations around 1 Hz to 4 Hz which corresponds to the natural frequency of the whole vehicle and the modal analysis results of the system. The modes indicating the main orders of the vehicle are all excited.

The vibration transmissibility curve can reflect that the existing damper parameters have a certain vibration-isolation effect. It can isolate most of the vibration transmitted from the ground and reduce the self-excited vibration of the IWM. The vibration transmissibility is -20 dB near 4 Hz, and each point is below -40 dB after 10 Hz.

According to the input vibration transmission of right middle wheel in Figure 17, the vibration transfer rate at the excitation point of the mass center is slightly higher than that of the right rear wheel. The reason for this is that the right middle wheel is closer to the mass center and has slightly weaker vibration isolation. The above two vibration transmissibility curves are similar. The difference is that the right rear-wheel input vibration-transmissibility curve is low (around 0.85 Hz). In addition, after the input vibration of the mid-wheel motor, the vibration transmissibility is the lowest at the left rear response point, followed by the left front response point, followed by the mass center and, finally, the right rear and right front.

The input vibration transfer of the right front wheel in Figure 18 is also different from the previous two. At 0.1 Hz, the vibration transmissibility of the right rear wheel is the lowest, followed by the mass center response point, followed by the left rear response point, the left front response point, and, finally, the right front response point. The vibration transmissibility of the right front response point is -0.7 dB at 0.1 Hz. Then, the vibration transmissibility increases with frequency within 1 Hz.

The right rear-wheel, right middle-wheel, and right front-wheel input vibration transmissions are repeatedly higher than 0 dB between 1 and 10 Hz. They do not have vibration damping capability under the above conditions. In order to study the influence of suspension stiffness on vibration transmission rate and improve the suspension vibration damping ability, multiple groups of stiffness are changed for vibration transmission analysis.

Figure 19 selects the mass center of the vehicle body as the excitation point. It can be understood from the figure that, with the decrease in stiffness, the vibration isolation performance of the system has a certain improvement. And with the decrease in stiffness, each formant is advanced. In summary, the stiffness mainly affects the vibration transmissibility in the mid-frequency range. If the damping performance in the mid-frequency range needs to be optimized, the stiffness should be reduced appropriately.

As shown in Figure 20, when the suspension stiffness is 55 N/mm, the vibration transmissibility of the right front wheel is improved in the mid-frequency region. At the same time, the vibration transmissibility is decreased.

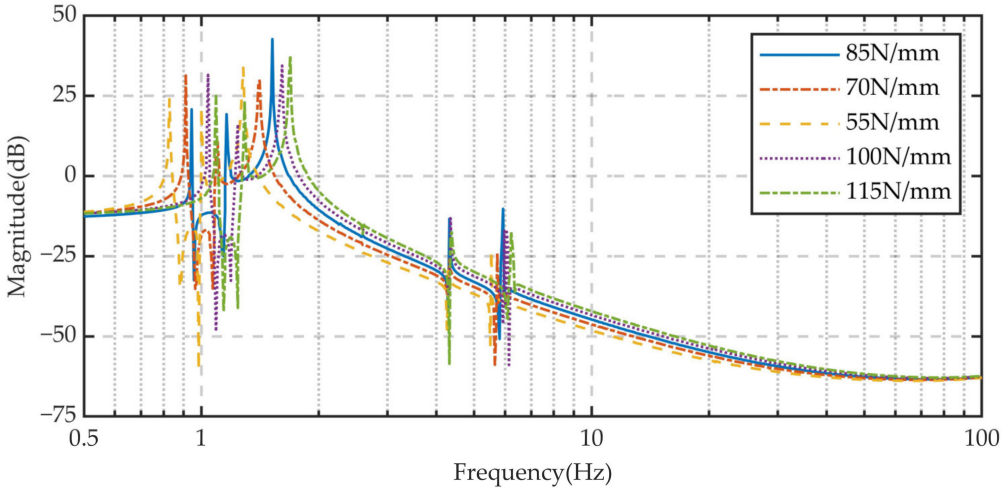


Figure 19. Input vibration transmission of the right front wheel with variable stiffness.

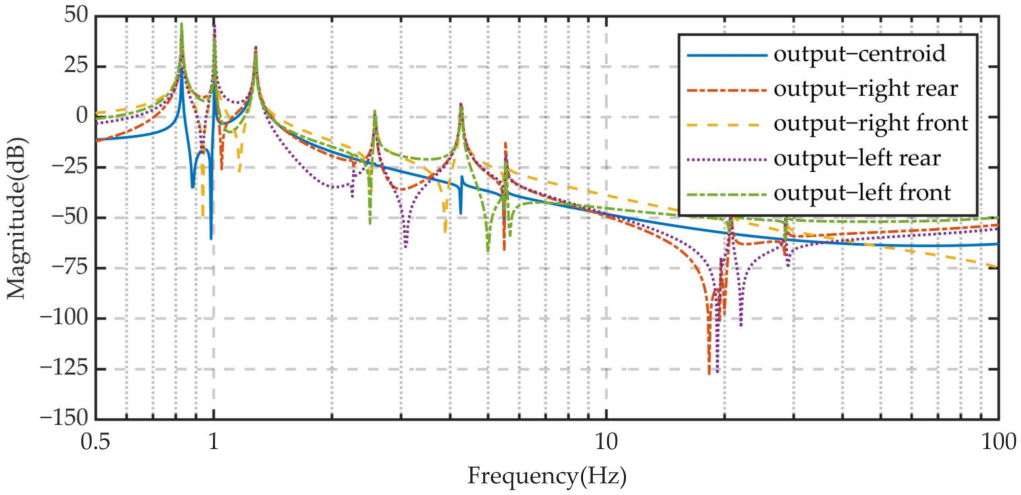


Figure 20. Input vibration transmission of right front wheel with a stiffness of 55 N/mm.

As shown in Figures 21 and 22, the vibration transmission is suppressed to varying degrees at the resonance peaks in each mode (set damping). As the vibration transmission rate decreases, the vibration-isolation performance improves. In the vertical direction, the human body is sensitive to the range of 4–8 Hz. In Figure 22, for example, the vibration transmission rate of the mass center starts from −29.1 dB down to −35.5 dB (4.2 Hz) in the interval of 4–8 Hz. And then the vibration transmission rate increases to −29.0 dB (4.4 Hz) and finally decreases to −39.9 dB. Equation (16) can determine that the road spectrum excitation is reduced by 97–99% at the center-of-mass position of the vehicle after multi-stage vibration reduction under the existing parameters.

$$L = 20\lg\left|\frac{a_o}{a_I}\right| \tag{16}$$

where L is the transmissibility ratio, a_o is the vibration output, and a_I is the vibration input.

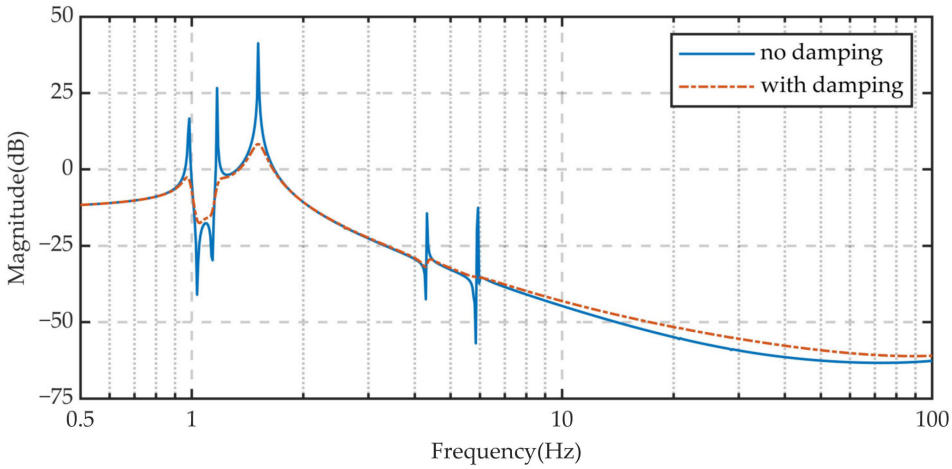


Figure 21. Vibration transmissibility comparison with or without damping.

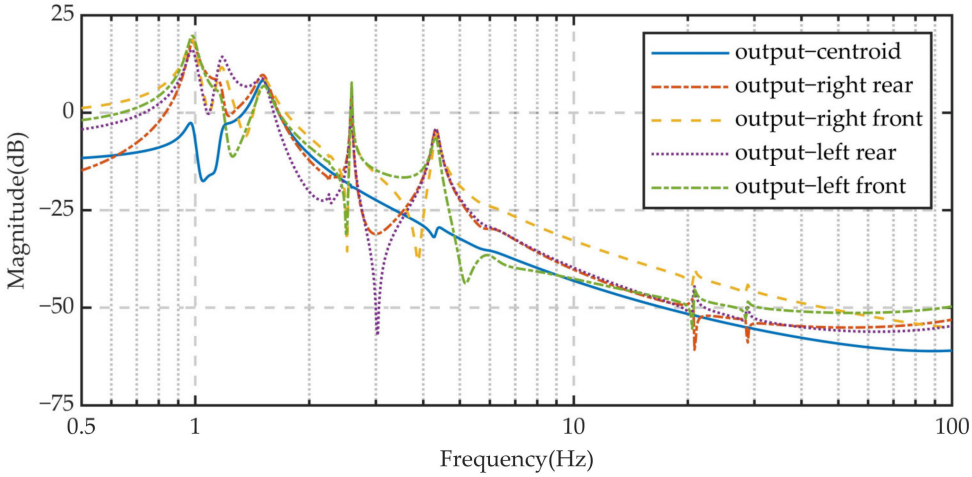


Figure 22. Rigidity of 85 N/mm right front wheel-input damped-vibration transmission.

4.2. Road Spectrum Model Establishment and Excitation Input

When studying the vibration models of the IWM and their vehicles, road excitation is usually the only external input in the vibration system. Choosing an appropriate road excitation model can make the simulation results more suitable for the actual situation.

In the field of vehicles, the road roughness IRI (International Roughness Index) value is usually used to reflect the road conditions and the excitation input for study vehicle vibration problems [42,43].

Under actual driving conditions, pavement excitation is generally a random process. Power spectral density (PSD) is generally used as a statistic of pavement excitation in research [44,45]. Through the measurement of the actual road surface, the roughness data of the road surface can be obtained, and the power spectrum of the working road surface of the vehicle can be obtained by spectrum analysis according to the data. The pavement power spectral density is used as the fitted expression (vehicle vibration input–road surface flatness representation) by the following equation [46,47]:

$$G_q(n) = G_q(n_0)\left(\frac{n}{n_0}\right)^{-w} \tag{17}$$

where n is the spatial frequency, m^{-1}, and the wavelength, w, which means the number of wavelengths per meter; n_0 is the reference spatial frequency; and $G_q(n)$ is the power spectral density of the pavement surface, which is called the pavement roughness coefficient. The unit is $m^2/m^{-1} = m^3$.

There are four commonly used methods for generating random excitation single-point time-domain models with random excitation of pavement unevenness: white noise method, harmonic superposition method, PSD discrete sampling method, and discrete time-series method. Among them, the white noise method has the characteristics of stability, fast simulation speed and less calculation. In this paper, the white noise method is used in the unevenness function.

According to the equation of the white noise method, the time-domain model of the single-wheel pavement excitation, q(t), is as follows:

$$\dot{y}_0 = -2\pi f_0 y_0(t) + 2\pi n_0 \sqrt{G_0(n_0) v_0} w(t) \tag{18}$$

where f_0 is the cut-off frequency of the pavement, and $f_0 = 0.011 m^{-1}$; $w(t)$ is the filtered white noise time-domain function; and v_0 is the vehicle speed.

The corresponding simulation model is established according to Equations (17) and (18), using Simulink. The completed Simulink model is shown in Figure 23.

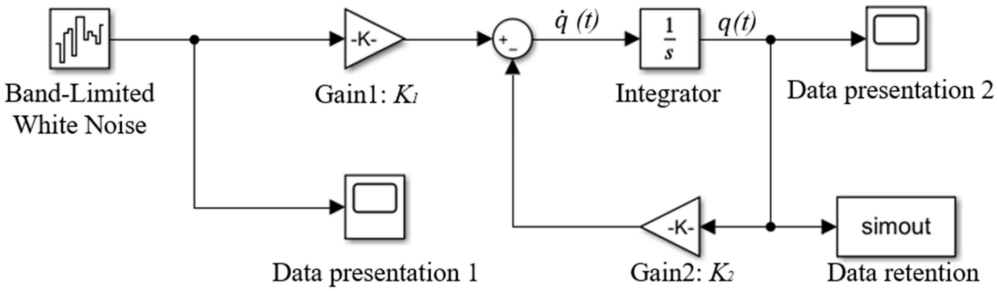


Figure 23. Simulink simulation model of random pavement.

Figure 24 shows the power spectrum characteristics of pavement roughness. The colored lines from bottom to top are the displacement power spectral density lines from A to G pavement grades. Taking the C-grade road surface as an example, the displacement power spectral density roughly falls between the B and D lines.

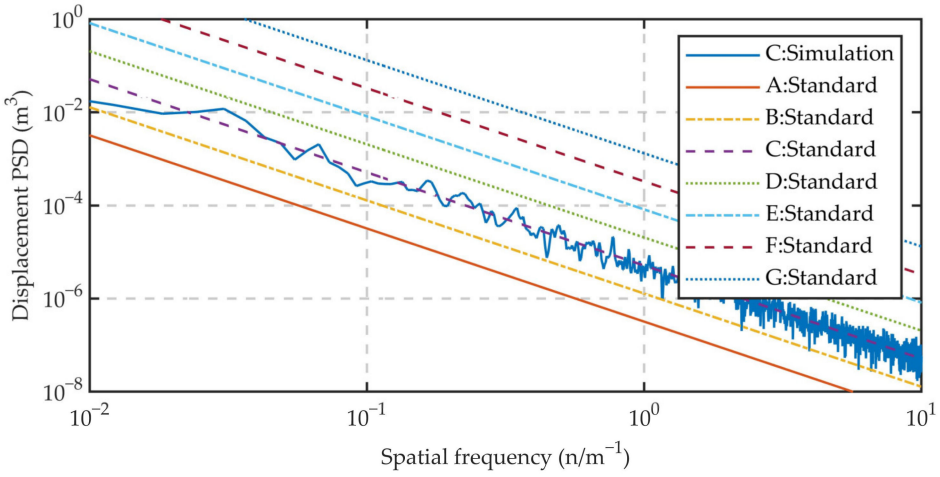


Figure 24. Power spectral characteristics of road-surface roughness.

4.3. Time-Domain Characteristic Analysis

The vehicle time-domain characteristics can reflect the vehicle dynamics performance under different simulated road spectrum conditions. The road spectrum is generated in MATLAB. It is used to simulate the vehicle driving on the road. As shown in Figure 7, the ground represents the simulated ground (depicted by a mass block). The time–displacement data generated in MATLAB are imported into the ground unit in ADAMS. The ground

unit then moves vertically over time. This method allows the time–displacement excitation generated in MATLAB to be applied to each tire through the ground unit. Then, dynamical parameters such as the acceleration, velocity, and displacement of each key part can be obtained in ADAMS.

For example, the time–displacement function of the C-class road surface is generated in MATLAB with a speed of 10 m/s. To ensure the spectral accuracy of the output spectrum, the white noise sampling interval is set to 0.001 s, and the total sampling time is 50 s. During vehicle operation, the front wheels on both sides of a six-wheeled vehicle traverse a particular section of the road first, followed by the middle wheels and, finally, the rear wheels. As a result, the simulated road surface will exhibit a translation, as shown in Figure 25, occurring at constant time intervals. For the narrow width of the vehicle and calculation convenience, the random road surface excitations for both the left and right wheels are represented using these curves. Then, import them into ADAMS for time-domain simulation analysis. The simulation time is 10 s. As shown in Figure 25, it is the displacement–time function of each tire under C-class road.

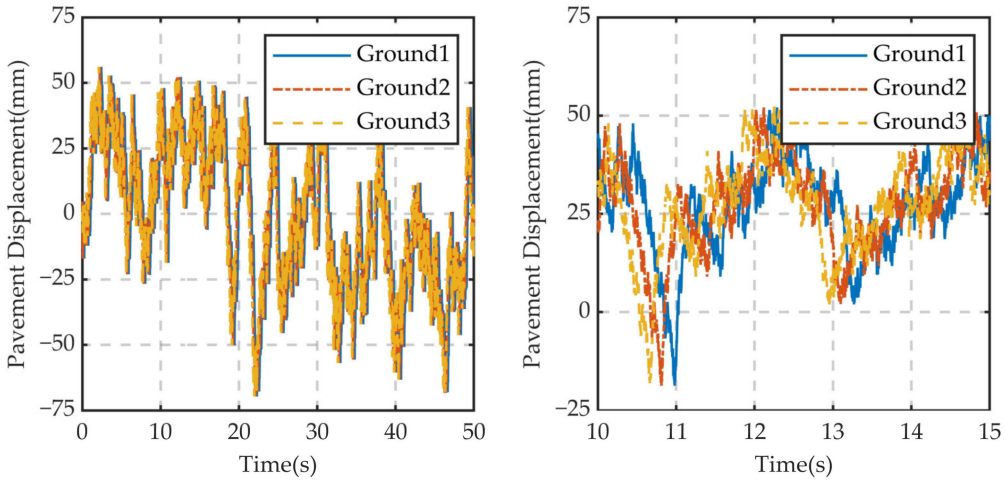


Figure 25. Displacement–time curve on a C-class road surface for different tires.

As shown in Figure 26, the acceleration is up to 1.671 m/s^2. The acceleration is significantly reduced. The graph can more intuitively reflect the actual acceleration–time graph of the mass center. In Figure 27, the maximum velocity of the mass center at 10 m/s is 0.125 m/s. From Figure 28, the maximum displacement of the mass center at 10 m/s is about 40 mm.

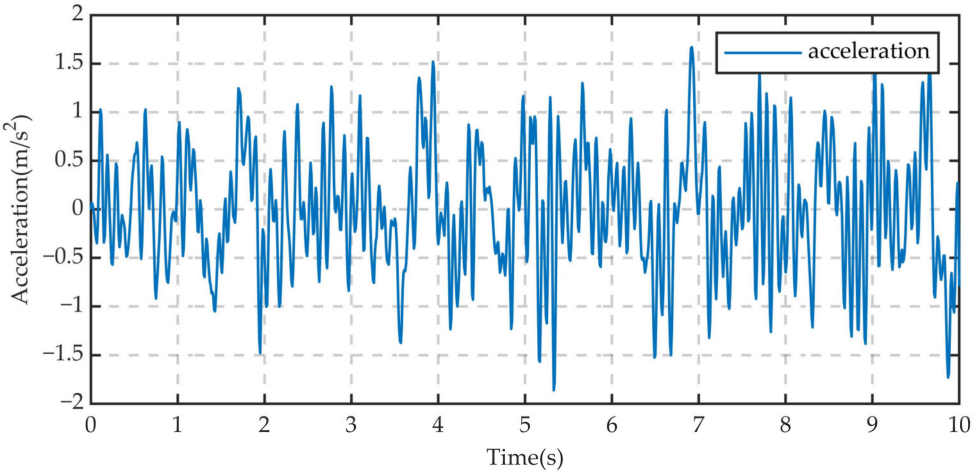


Figure 26. Acceleration–time curve of the car body center of mass at 10 m/s on the C-class road.

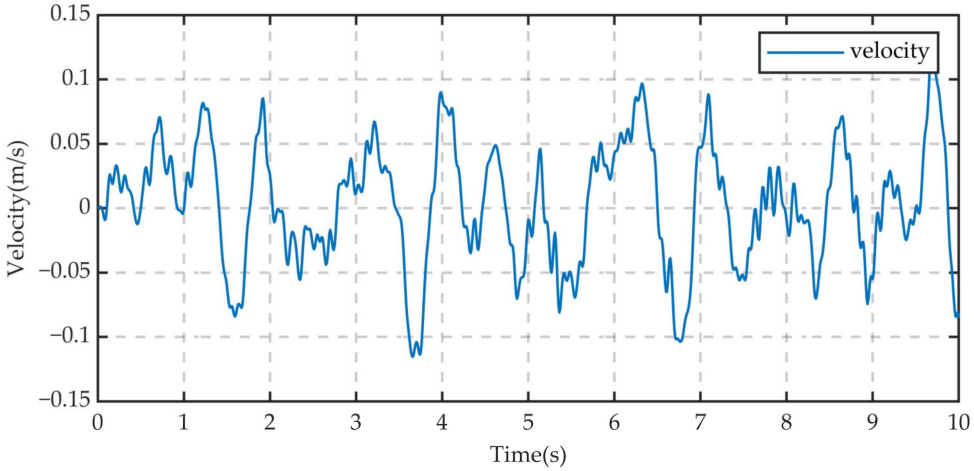


Figure 27. Velocity–time curve of the vehicle body center of mass at 10 m/s on the C-class road.

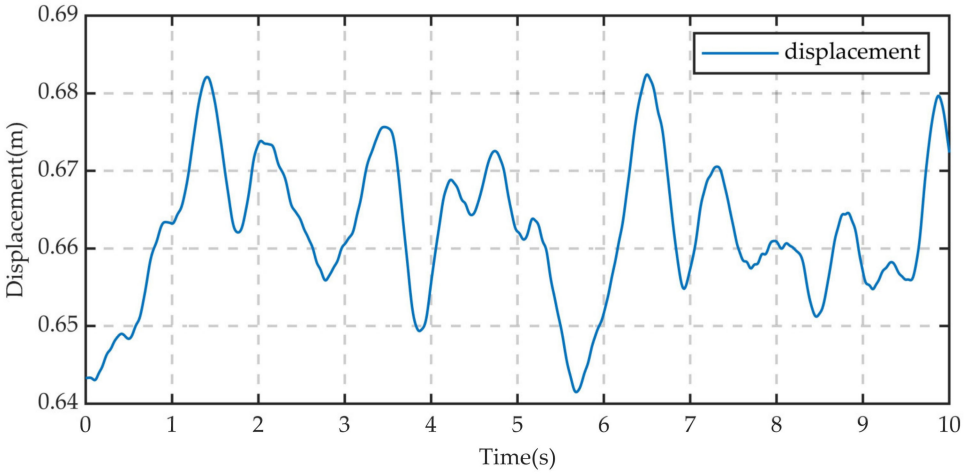


Figure 28. Displacement–time curve of the vehicle body center of mass at 10 m/s on the C-class road.

Then, acceleration and velocity measurements are performed on the remaining key parts. It can be seen from the measurement data that the average value of the key accelerations and speeds of the vehicle body, except for the mass center, is significantly higher than the mass center, because the stability of the mass center is higher. The acceleration of the right rear wheel, right front wheel, left rear wheel, and left front wheel reaches a maximum of 6.977 m/s^2, which is about four times the acceleration of the mass center.

The 30 m/s road spectrum function for C-Class pavement and the 10 m/s road spectrum function for E-Class pavement are generated in MATLAB and imported into ADAMS for simulation of acceleration, velocity, and other parameters. Figures 26 and 29, Figures 30–42, respectively, present the acceleration–time curves at various measurement reference points under different vehicle speeds and road conditions. The selection of measurement reference points is explained in Table 8.

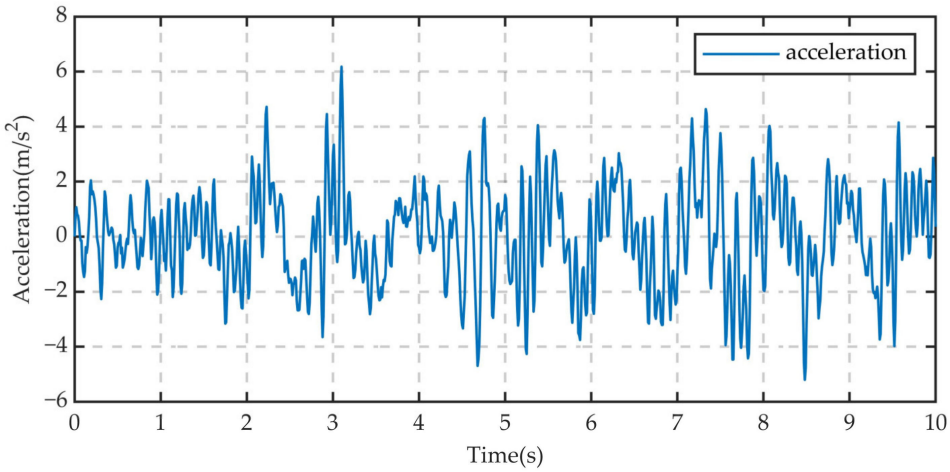


Figure 29. Acceleration–time curve of the car body's right rear at 10 m/s on the C-class road.

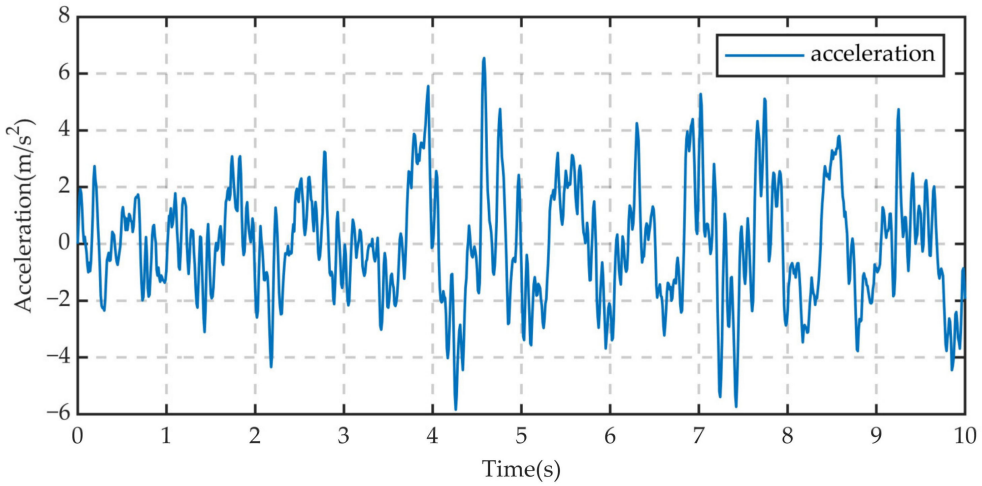


Figure 30. Acceleration–time curve of the car body's right front at 10 m/s on the C-class road.

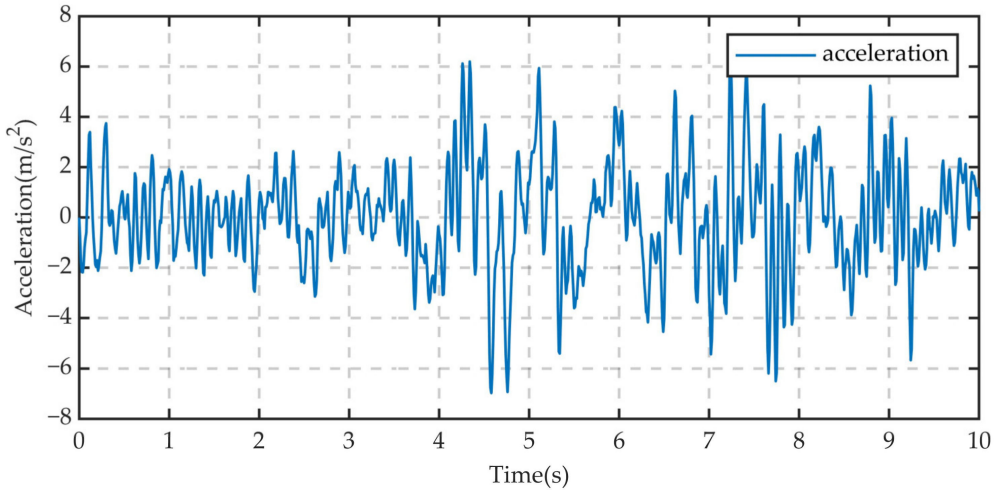


Figure 31. Acceleration–time curve of the car body's left rear at 10 m/s on the C-class road.

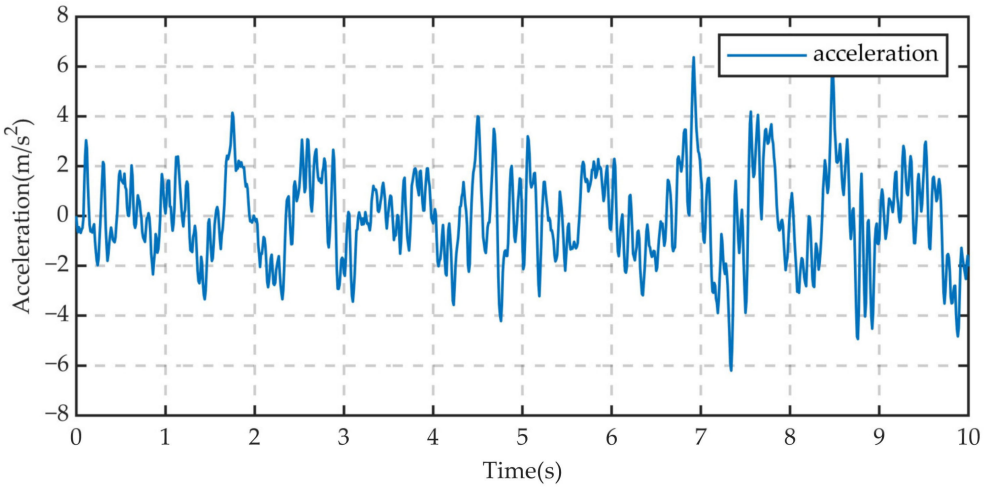


Figure 32. Acceleration–time curve of the car body's left front at 10 m/s on the C-class road.

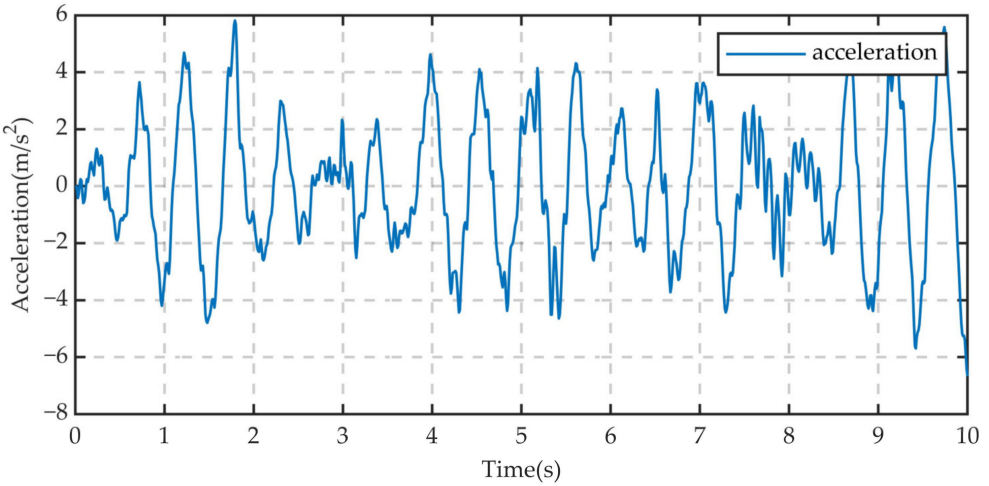


Figure 33. Acceleration–time curve of the car body center of mass at 30 m/s on the C-class road.

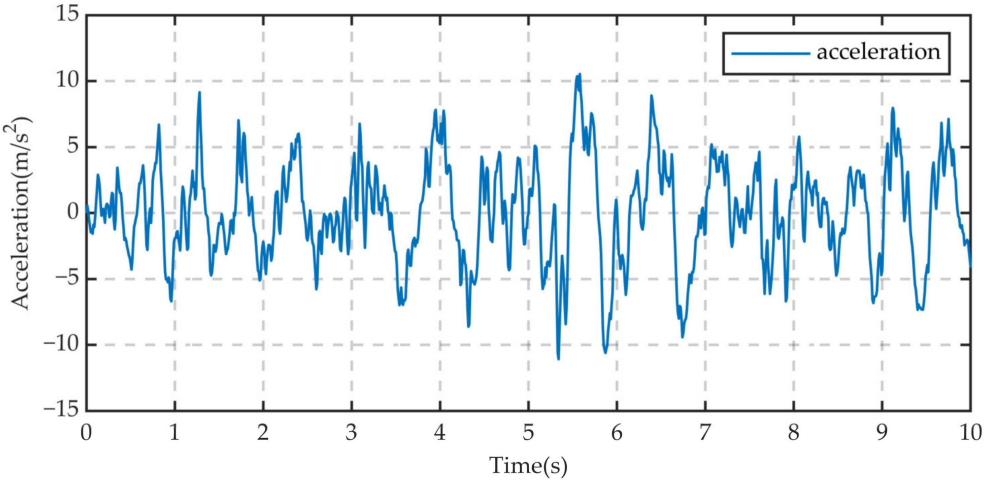


Figure 34. Acceleration–time curve of the car body's right rear at 30 m/s on the C-class road.

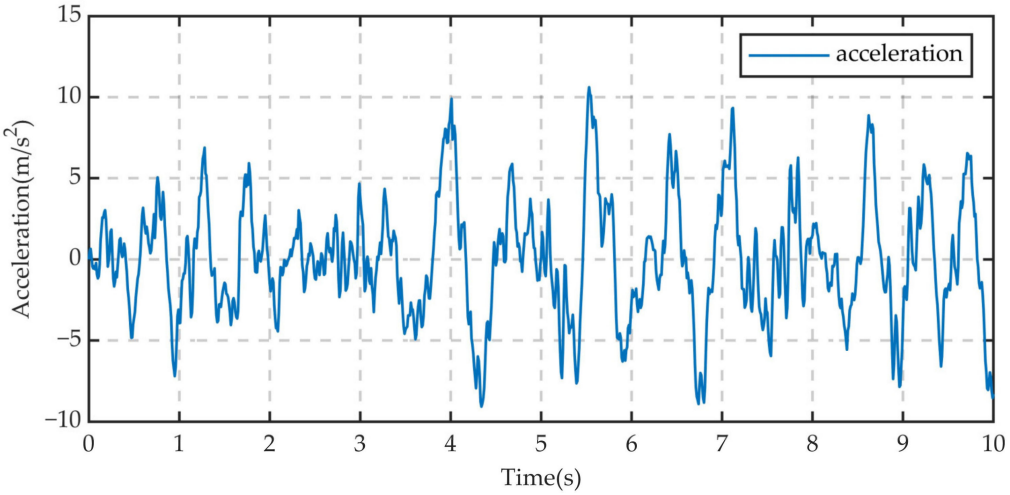


Figure 35. Acceleration–time curve of the car body's right front at 30 m/s on the C-class road.

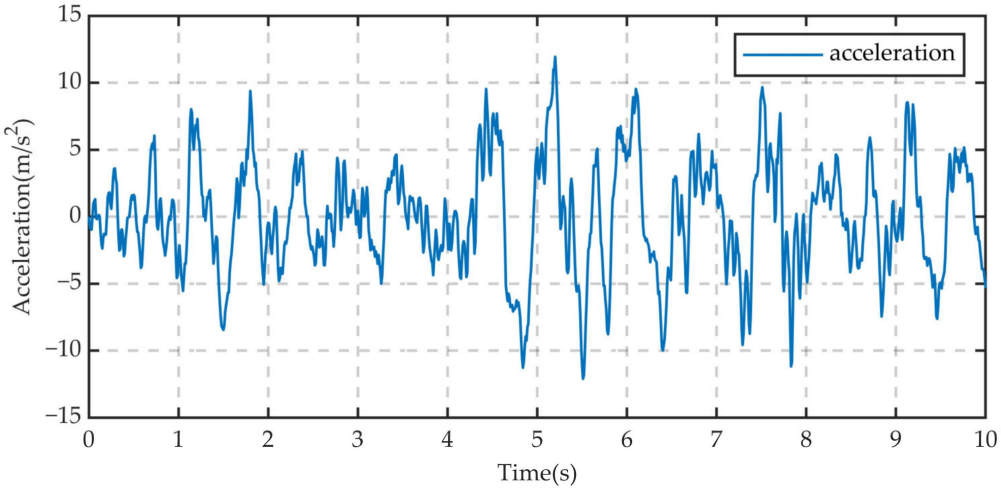


Figure 36. Acceleration–time curve of the car body's left rear at 30 m/s on the C-class road.

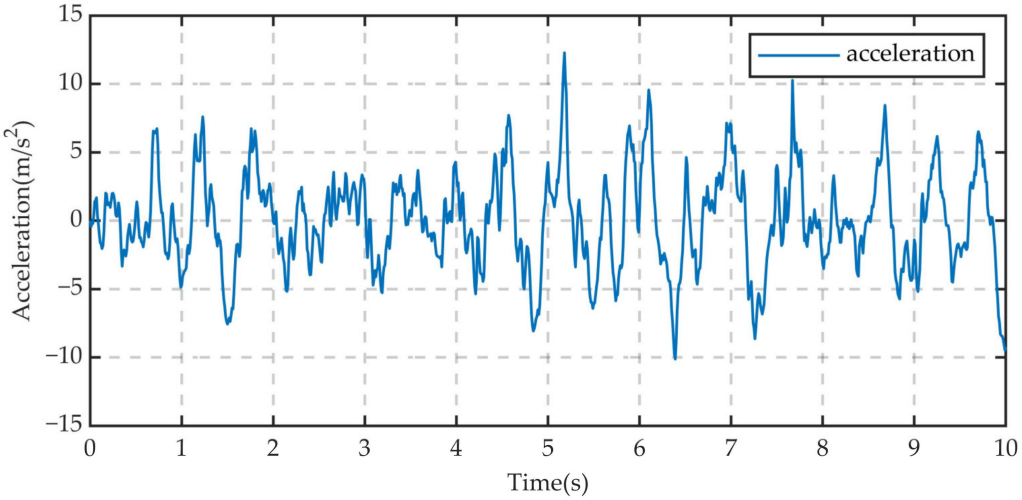


Figure 37. Acceleration–time curve of the car body's left front at 30 m/s on the C-class road.

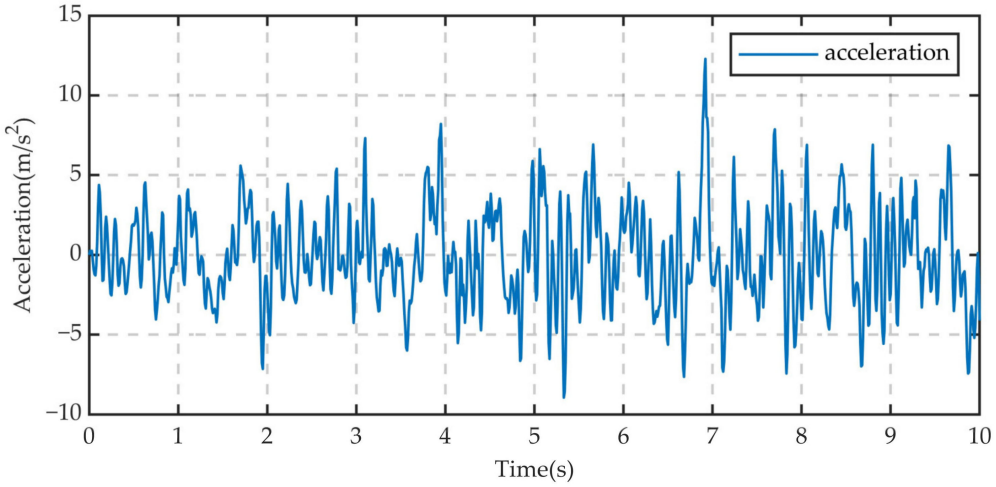


Figure 38. Acceleration–time curve of the car body center of mass at 10 m/s on the E-class road.

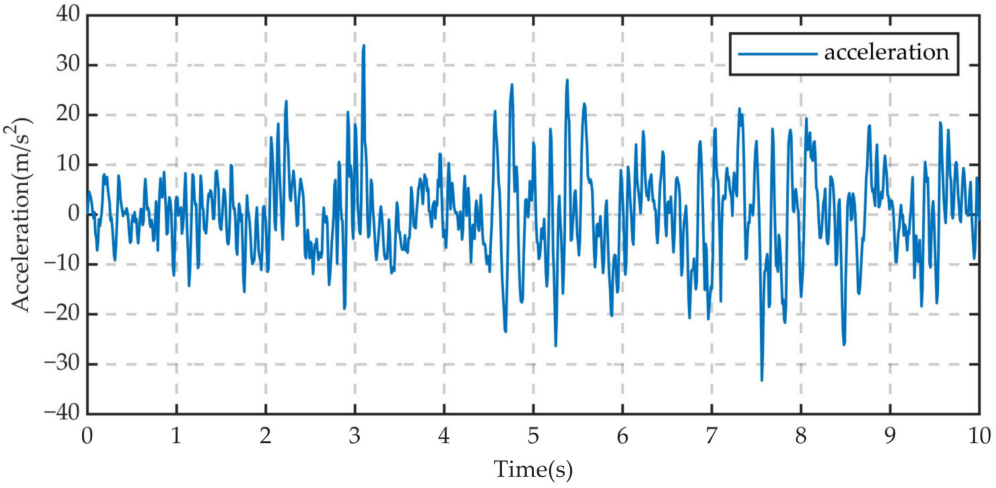


Figure 39. Acceleration–time curve of the car body's right rear at 10 m/s on the E-class road.

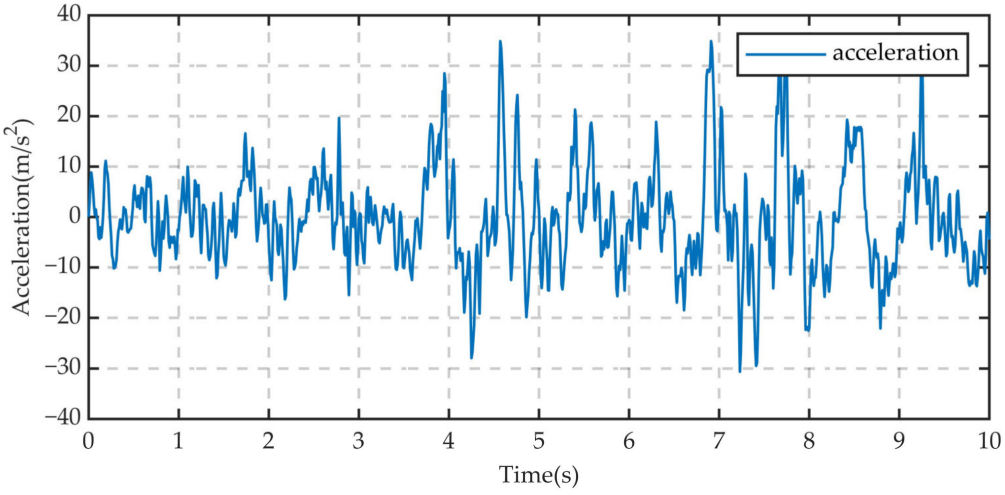


Figure 40. Acceleration–time curve of the car body's right front at 10 m/s on the E-class road.

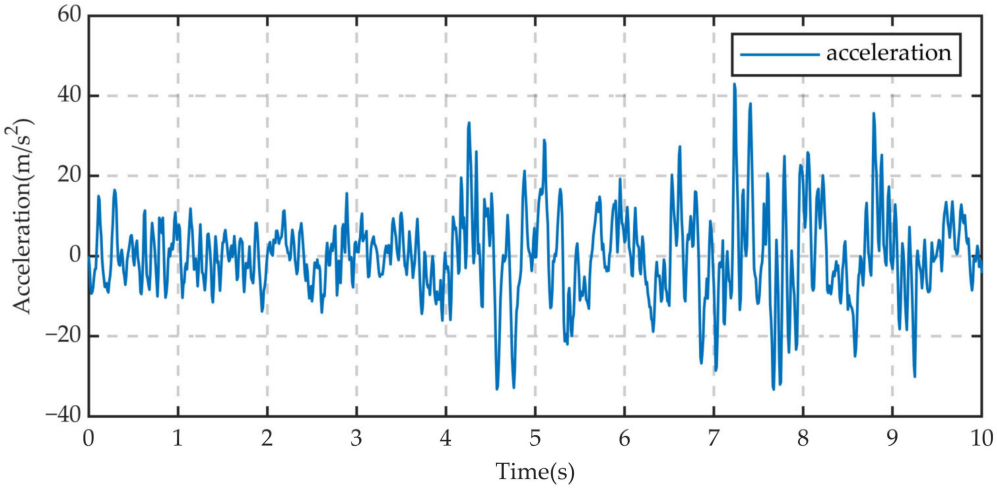


Figure 41. Acceleration–time curve of the car body's left rear at 10 m/s on the E-class road.

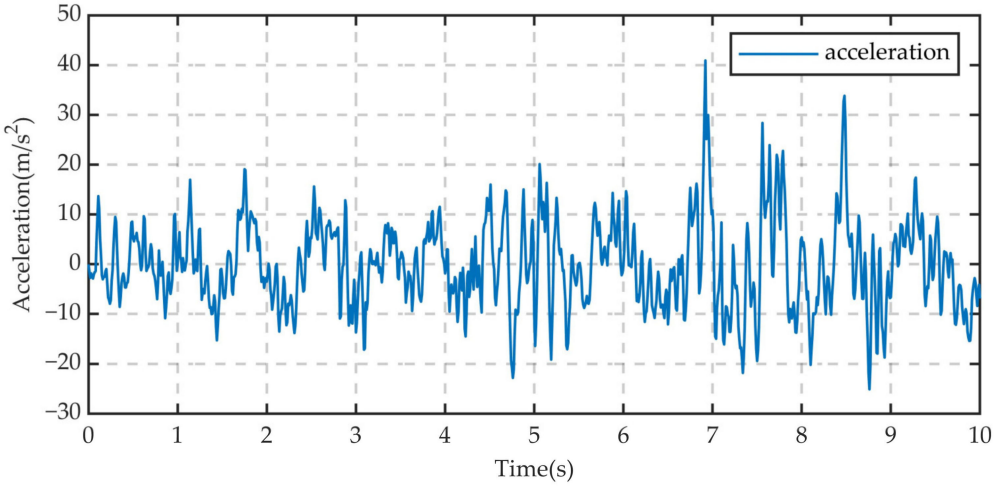


Figure 42. Acceleration–time curve of the car body's left front at 10 m/s on the E-class road.

From Figures 26 and 29–42, it can be seen that the acceleration at the vehicle's center of mass is the lowest among the five measurement reference points under the same speed and road conditions. Since each tire is driven by its respective IWM and the road positions encountered by the tires vary, the acceleration–time curves obtained from different measurement reference points differ. Table 9 also shows that the peak acceleration and acceleration RMS values at different measurement reference points vary, although they fluctuate within a reasonable range. It is evident that the increase in speed and more severe pavement conditions lead to higher acceleration at each response point. Moreover, the increase in acceleration when moving from C-class to E-class pavement is more significant than the increase caused by speeding up from 10 m/s to 30 m/s on C-class pavement. Additionally, it is worth noting that, as the vehicle speed increases, the ratio of acceleration difference between the vehicle's center of mass and other measurement reference points decreases. However, when the pavement class changes from C to E, this ratio remains relatively unchanged. This indicates that the increase in speed causes the measurements at different reference points to converge.

Table 9. Main parameters of vehicle system in time domain.

No.	Road Class	Speed (m/s)	Position	Peak Acceleration (m/s^2)	Acceleration RMS (m/s^2)
1	C class	10	Centroid	1.671	0.619
2		10	RR	6.180	1.750
3		10	RF	6.550	1.995
4		10	LR	6.977	2.075
5		10	LF	6.369	1.837
6		30	Centroid	6.673	2.399
7		30	RR	11.082	3.781
8		30	RF	10.612	3.641
9		30	LR	12.103	4.113
10		30	LF	12.286	3.539
11	E class	10	Centroid	12.291	2.970
12		10	RR	33.973	8.802
13		10	RF	34.871	9.917
14		10	LR	42.979	10.463
15		10	LF	40.914	8.729

This section also aims to ensure the comfort of the occupants in the car (driven by IWM) under high-speed driving and harsher driving conditions in the field.

5. Conclusions

Special vehicles driven by direct-drive IWMs have faced complex and harsh working conditions for a long time. Insufficient understanding of the natural characteristics and transfer action laws of such special vehicles constrains further improvement of the dynamic performance. This work completes the following work:

1. Proposes a system-integrated modeling strategy and method for dynamic design of IWM.

In order to accurately design the IWM in service under complex working conditions, this paper proposes a system integration modeling strategy for the dynamic design of IWM and builds an integrated dynamic model of environment–hub unit–suspension–vehicle body–vibration isolator–vibration-isolated body with global system characteristics.

2. Constructs the key subsystem of IWM bearing unit and the vehicle dynamics model.

Aiming at the dynamics modeling problem of key unit subsystems (such as IWM bearing unit subsystem, suspension subsystem, and tire subsystem), a dynamic modeling method of key units for special vehicles is proposed in the system-integrated dynamics modeling. The equivalent multi-body model of several types of IWM bearing units and the equivalent stiffness model of the tire system are established, and the dynamic characteristic parameters of the key units are identified by theoretical means. Based on this, vehicle system dynamic models were developed and cross-validated between MATLAB and ADAMS to ensure their robustness and accuracy. The dynamic modeling approaches using MATLAB and ADAMS proposed in this paper each have their strengths. The MATLAB model offers more thorough simplification, resulting in faster computation speeds and higher efficiency. On the other hand, the ADAMS model provides a more comprehensive consideration of various factors, with more components and degrees of freedom, allowing for a detailed representation of vehicle dynamics. However, the ADAMS model faces challenges, such as complex modeling and lower computational efficiency. Furthermore, the parameters obtained in MATLAB and ADAMS also serve as a theoretical foundation for the design work of special vehicles driven by direct-drive IWMs.

3. Establishes a multi-source dynamic load characterization method and analyzed the vibration characteristics of the vehicle.

Aiming at solving the problem of analyzing multi-source dynamic load characteristics, this paper proposes a characterization method for dynamic load excitation under different road conditions and establishes a mechanical characteristic evaluation standard considering the dynamic characteristics of IWM. The natural frequency of the vehicle system is 1.47 Hz, and the vehicle mode is mainly distributed around 1–4 Hz. In terms of vehicle vibration transmission, each frequency band has a certain vibration reduction and isolation capability for the IWM and the vehicle system. The vibration input can be reduced by 97–99% after multi-stage vibration reduction. In terms of time domain, the vehicle faces different road surfaces and different vehicle speeds. The maximum RMS (Root Mean Square) value is 10.463 m/s^2, and the minimum RMS value is 0.619 m/s^2.

This study aims to improve the dynamic performance of special vehicles driven by direct-drive IWMs and enhance passenger comfort by establishing dynamic models to explore the inherent characteristics and transmission mechanisms of these vehicles. In the future, the content of the system-integrated modeling strategy and methods for the dynamic design of IWMs will be further enriched. Research will focus on the vibration characteristics of special vehicles driven by direct-drive IWMs under different environmental conditions to enhance vehicle adaptability to various environments. New types of isolators will be designed to reduce localized vibrations in the vehicle, and the structure of the IWM will be optimized to improve the dynamic characteristics within the wheel. The key subsystem modeling, vehicle dynamics modeling, and vibration characteristic analysis presented in this paper provide a solid foundation for future research and exploration.

Author Contributions: Conceptualization, X.L., J.W. and W.J.; data curation, X.L.; formal analysis, X.L.; funding acquisition, J.W.; investigation, R.L. and Y.Z.; methodology, X.L., J.C., W.J. and J.W.; project administration, J.W.; resources, J.W.; visualization, J.C.; writing—original draft, X.L. All authors have read and agreed to the published version of the manuscript.

Funding: This work was supported by the National Natural Science Foundation of China (No. 52305107, No. 52075193, and No. 52275112), the Guangdong Basic and Applied Basic Research Foundation (No. 2024A1515010127), the National Key R&D Program of China (No. 2020YFB2007300 and No. 2020YFB2007601), and the National Science and Technology Major Project of China (No. 2017ZX02101007-002).

Data Availability Statement: Data are contained within the article.

Conflicts of Interest: Authors Rui Liu and Yihui Zhao were employed by the company Inner Mongolian First Machinery Group Co., Ltd. The remaining authors declare that the research was conducted in the absence of any commercial or financial relationships that could be construed as a potential conflict of interest. The Inner Mongolian First Machinery Group Co., Ltd. had no role in the design of the study; in the collection, analyses, or interpretation of data; in the writing of the manuscript, or in the decision to publish the results.

Abbreviations

The following abbreviations are used in this paper:

IWM	in-wheel motor
MM	magnet motor
NVH	noise, vibration, and harshness
WBV	whole-body vibration
MMG	motor magnetic gap
DDUGV	Distributed-Drive Unmanned Ground Vehicle
DOF	degree of freedom
CAE	Computer-Aided Engineering
IRI	International Roughness Index
PSD	power spectral density
RMS	Root Mean Square

References

1. Satoshi, M. Innovation by in-wheel-motor drive unit. *Veh. Syst. Dyn.* **2012**, *50*, 807–830.
2. Wagh, K.; Dhatrak, P. A review on powertrain subsystems and charging technology in battery electric vehicles: Current and future trends. *Proc. Inst. Mech. Eng. Part D J. Automob. Eng.* **2022**, *236*, 479–496. [CrossRef]
3. Kumar, P.; Chakrabarty, S. Total cost of ownership analysis of the impact of vehicle usage on the economic viability of electric vehicles in India. *Transp. Res. Rec.* **2020**, *2674*, 563–572. [CrossRef]
4. Li, Z.; Zheng, L.; Ren, Y.; Li, Y.; Xiong, Z. Multi-objective optimization of active suspension system in electric vehicle with In-Wheel-Motor against the negative electromechanical coupling effects. *Mech. Syst. Signal Process.* **2019**, *116*, 545–565. [CrossRef]
5. Deepak, K.; Frikha, M.A.; Benômar, Y.; El Baghdadi, M.; Hegazy, O. In-Wheel Motor Drive Systems for Electric Vehicles: State of the Art, Challenges, and Future Trends. *Energies* **2023**, *16*, 3121. [CrossRef]
6. He, S.; Fan, X.; Wang, Q.; Chen, X.; Zhu, S. Review on torque distribution scheme of four-wheel in-wheel motor electric vehicle. *Machines* **2022**, *10*, 619. [CrossRef]
7. Qatu, M.; Sirafi, M.; Johns, F. Robustness of powertrain mount system for noise, vibration and harshness at idle. *Proc. Inst. Mech. Eng. Part D J. Automob. Eng.* **2002**, *216*, 805–810. [CrossRef]
8. Nagaya, G.; Wakao, Y.; Abe, A. Development of an in-wheel drive with advanced dynamic-damper mechanism. *JSAE Rev.* **2003**, *24*, 477–481. [CrossRef]
9. Yane, Z.; Jianwu, Z.; Xu, H. Design and study on the dynamic-damper mechanism for an in-wheel motor individual drive electric vehicle. *Mech. Sci. Technol.* **2008**, *27*, 395.
10. Ahmad, I.; Ge, X.; Han, Q.L. Decentralized dynamic event-triggered communication and active suspension control of in-wheel motor driven electric vehicles with dynamic damping. *IEEE/CAA J. Autom. Sin.* **2021**, *8*, 971–986. [CrossRef]
11. Yoon, D.S.; Choi, S.B. Adaptive Control for Suspension System of In-Wheel Motor Vehicle with Magnetorheological Damper. *Machines* **2024**, *12*, 433. [CrossRef]
12. Nam, K.; Fujimoto, H.; Hori, Y. Lateral stability control of in-wheel-motor-driven electric vehicles based on sideslip angle estimation using lateral tire force sensors. *IEEE Trans. Veh. Technol.* **2012**, *61*, 1972–1985.
13. Zhang, H.; Wang, R.; Wang, J. Robust H∞ Output-Feedback Yaw Control for In-Wheel Motor-Driven Electric Vehicles with Differential Steering. In *Robust Gain-Scheduled Estimation and Control of Electrified Vehicles via LPV Technique*; Springer Nature Singapore: Singapore, 2023; pp. 131–152.
14. Belrzaeg, M.; Ahmed, A.A.; Khaleel, M.M.; Alsharif, A.; Rahmah, M.M.; Alarga, A.S.D. Suspension system control process for Buses with In-Wheel Motors. *Eng. Proc.* **2023**, *29*, 4. [CrossRef]
15. Rudiger, H. Technical Potential of in-Wheel Motors. *ATZ Worldw.* **2012**, *114*, 4–9.
16. Li, C.; Guo, X.; Fu, J.; Fu, W.; Liu, Y.; Chen, H.; Wang, R.; Li, Z. Design and analysis of a novel double-stator double-rotor motor drive system for in-wheel direct drive of electric vehicles. *Machines* **2021**, *10*, 27. [CrossRef]
17. Chan, C.C. An overview of electric vehicle technology. *Proc. IEEE* **1993**, *81*, 1202–1213. [CrossRef]
18. Matsugaura, S.; Kawakami, K.; Shimizu, H. Advanced Direct Drive System for New Concept Electric Vehicle "KAZ". In Proceedings of the 18th International Electric Vehicle Symposium (EVS18), Berlin, Germany, 20–24 October 2001.
19. Yoshida, H.; Shimizu, H. Transportation and Safety in Japan: "Ellica"-the 370 km/h Maximum Speed Electric Vehicle. *IATSS Res.* **2005**, *29*, 75. [CrossRef]
20. Zhao, Z.; Taghavifar, H.; Du, H.; Qin, Y.; Dong, M.; Gu, L. In-wheel motor vibration control for distributed-driven electric vehicles: A review. *IEEE Trans. Transp. Electrif.* **2021**, *7*, 2864–2880. [CrossRef]
21. Qin, Y.; Rath, J.J.; Hu, C.; Sentouh, C.; Wang, R. Adaptive nonlinear active suspension control based on a robust road classifier with a modified super-twisting algorithm. *Nonlinear Dyn.* **2019**, *97*, 2425–2442. [CrossRef]
22. Qin, Y.; Wang, Z.; Xiang, C.; Hashemi, E.; Khajepour, A.; Huang, Y. Speed independent road classification strategy based on vehicle response: Theory and experimental validation. *Mech. Syst. Signal Process.* **2019**, *117*, 653–666. [CrossRef]
23. Zirkohi, M.M.; Lin, T.C. Interval type-2 fuzzy-neural network indirect adaptive sliding mode control for an active suspension system. *Nonlinear Dyn.* **2015**, *79*, 513–526. [CrossRef]
24. Qin, Y.; He, C.; Shao, X.; Du, H.; Xiang, C.; Dong, M. Vibration mitigation for in-wheel switched reluctance motor driven electric vehicle with dynamic vibration absorbing structures. *J. Sound Vib.* **2018**, *419*, 249–267. [CrossRef]
25. Shao, X.; Naghdy, F.; Du, H.; Qin, Y. Coupling effect between road excitation and an in-wheel switched reluctance motor on vehicle ride comfort and active suspension control. *J. Sound Vib.* **2019**, *443*, 683–702. [CrossRef]
26. Múčka, P. International roughness index thresholds based on whole-body vibration in passenger cars. *Transp. Res. Rec.* **2021**, *2675*, 305–320. [CrossRef]
27. Kumar, R.; Sharma, R.; Kumar, V.; Khan, A.A. Predictors of whole-body vibration exposure among Indian bus and truck drivers. *J. Phys. Conf. Ser.* **2021**, *1854*, 012033. [CrossRef]
28. Svendenius, J.; Gäfvert, M. A semi-empirical dynamic tire model for combined-slip forces. *Veh. Syst. Dyn.* **2006**, *44*, 189–208. [CrossRef]
29. Luo, Y.; Tan, D. Study on the dynamics of the in-wheel motor system. *IEEE Trans. Veh. Technol.* **2012**, *61*, 3510–3518.
30. Jin, X.; Wang, J.; He, X.; Yan, Z.; Xu, L.; Wei, C.; Yin, G. Improving vibration performance of electric vehicles based on in-wheel motor-active suspension system via robust finite frequency control. *IEEE Trans. Intell. Transp. Syst.* **2023**, *24*, 1631–1643. [CrossRef]

31. Nah, J.; Yim, S. Vehicle stability control with four-wheel independent braking, drive and steering on in-wheel motor-driven electric vehicles. *Electronics* **2020**, *9*, 1934. [CrossRef]
32. Drexler, D.; Hou, Z. Simulation analysis on vertical vehicle dynamics of three in-wheel motor drive configurations. *Proc. Inst. Mech. Eng. Part D J. Automob. Eng.* **2023**, *238*, 2105–2119. [CrossRef]
33. Jin, X.; Wang, J.; Yan, Z.; Xu, L.; Yin, G.; Chen, N. Robust vibration control for active suspension system of in-wheel-motor-driven electric vehicle via μ-synthesis methodology. *J. Dyn. Syst. Meas. Control.* **2022**, *144*, 051007. [CrossRef]
34. Ma, Y.; Deng, Z.; Xie, D. Control of the active suspension for in-wheel motor. *J. Adv. Mech. Des. Syst. Manuf.* **2013**, *7*, 535–543. [CrossRef]
35. Liu, M.; Gu, F.; Zhang, Y. Ride comfort optimization of in-wheel-motor electric vehicles with in-wheel vibration absorbers. *Energies* **2017**, *10*, 1647. [CrossRef]
36. Lu, S.; Xu, X.; Wang, W. Coupling dynamic model of vehicle-wheel-ground for all-terrain distributed driving unmanned ground vehicle. *Simul. Model. Pract. Theory* **2023**, *128*, 102817. [CrossRef]
37. Wang, W.H.; Xu, X.J.; Xu, H.J.; Zhou, F.-L. Enhancing lateral dynamic performance of all-terrain vehicles using variable-wheelbase chassis. *Adv. Mech. Eng.* **2020**, *12*, 1–19. [CrossRef]
38. Jiang, Y.; Xu, X.; Zhang, L. Heading tracking of 6WID/4WIS unmanned ground vehicles with variable wheelbase based on model free adaptive control. *Mech. Syst. Signal Process.* **2021**, *159*, 107715. [CrossRef]
39. Zhang, C.; Chen, G.; Li, Z.; Qiu, X.; Guo, S. Design and control of a foldable and reconfigurable multi-terrain vehicle with variable wheelbase. *J. Mech. Robot.* **2023**, *15*, 024501. [CrossRef]
40. Yamada, S.; Beauduin, T.; Fujimoto, H.; Kanou, T.; Katsuyama, E. Active Model-Based Suppression of Secondary Ride for Electric Vehicles with In-Wheel Motors. *IEEE/ASME Trans. Mechatron.* **2022**, *27*, 5637–5646. [CrossRef]
41. Tseng, H.E.; Hrovat, D. State of the art survey: Active and semi-active suspension control. *Veh. Syst. Dyn.* **2015**, *53*, 1034–1062. [CrossRef]
42. Wang, F.; Easa, S. Analytical evaluation of ride comfort on asphalt concrete pavements. *J. Test. Eval.* **2016**, *44*, 1671–1682. [CrossRef]
43. Qin, Y.; Zhao, Z.; Wang, Z.; Li, G. Study of longitudinal–vertical dynamics for in-wheel motor-driven electric vehicles. *Automot. Innov.* **2021**, *4*, 227–237. [CrossRef]
44. Múčka, P. Proposal of road unevenness classification based on road elevation spectrum parameters. *J. Test. Eval.* **2016**, *44*, 930–944. [CrossRef]
45. Davis, B.R.; Thompson, A.G. Power spectral density of road profiles. *Veh. Syst. Dyn.* **2001**, *35*, 409–415. [CrossRef]
46. Kong, Y.; Zhao, D.; Yang, B.; Han, C.; Han, K. Non-fragile multi-objective static output feedback control of vehicle active suspension with time-delay. *Veh. Syst. Dyn.* **2014**, *52*, 948–968. [CrossRef]
47. Salehi, M.; Bamimohamadi, G. An enhanced adaptive neuro-fuzzy vehicle suspension control in different road conditions. *Int. J. Dyn. Control* **2019**, *7*, 701–712. [CrossRef]

Disclaimer/Publisher's Note: The statements, opinions and data contained in all publications are solely those of the individual author(s) and contributor(s) and not of MDPI and/or the editor(s). MDPI and/or the editor(s) disclaim responsibility for any injury to people or property resulting from any ideas, methods, instructions or products referred to in the content.